J. Fluid Mech. (2003), *vol.* 490, *pp.* 217–249.
DOI: 10.1017/S0022112003005238 Printed in the United Kingdom

Experimental investigation and numerical modelling of steep forced water waves

By H. BREDMOSE[1]†, M. BROCCHINI[2], D. H. PEREGRINE[3] AND L. THAIS[4]

[1]Department of Mechanical Engineering, Building 101E, Technical University of Denmark, DK-2800 Lyngby, Denmark

[2]Dipartimento di Ingegneria Ambientale, University of Genova, Via Montallegro 1, 16145 Genova, Italy

[3]School of Mathematics, University of Bristol, Bristol BS8 1TW, UK

[4]Laboratoire de Mécanique de Lille, Université des Sciences et Technologies de Lille, Cité Scientifique, 59655 Villeneuve d'Ascq Cedex, France

(Received 21 November 2001 and in revised form 2 April 2003)

Steep forced water waves generated by moving a rectangular tank are investigated both experimentally and numerically. Our main focus is on energetic events generated by two different types of external forcing. Horizontal motions are arranged to give wave impact on the sidewall. Steep standing waves forced by vertical acceleration can result in spectacular breaking modes similar to, and more energetic than, those reported by Jiang, Perlin & Schultz (1998, hereinafter J98). Among them we find thin sheets derived from sharp-crested waves, ('mode A' of J98) and the 'flat-topped' crest or 'table-top' breaker ('mode B' of J98). We report here on experimental observations of 'table-top' breakers showing remarkably long periods of free fall motion. Previously such breakers have only been observed in numerical computations. Both types of breakers often thin as they fall to give thin vertical sheets of water whose downward motion ends in either a small depression and a continuing smooth surface, or air entrainment to appreciable depths. Experimental results are compared graphically with numerical results of two theoretical models. One is an extended set of Boussinesq equations following Wei *et al.* (1995), which are successful up to wave slopes of $O(1)$. The other numerical comparison is with a fully nonlinear irrotational flow solver (Dold 1992) which can follow the waves to breaking.

1. Introduction

Violent water free-surface motions under gravity are a concern for many different human activities. In the context of coastal engineering, the impact of steep water waves can result in damage or collapse of structures. In particular, failure of vertical breakwaters and coastal defences has led to much attention being given to the pressure distribution which occurs when steep storm waves meet sea walls (e.g. Chan 1994; Zhang, Yue & Tanizawa 1996). Both experimental (Hattori, Arami & Yui 1994) and theoretical (Cooker & Peregrine 1992) studies have highlighted the fundamental role of the very large impact pressures which are impulsively exerted

† Present address: School of Mathematics, University of Bristol, Bristol BS8 1TW, UK.

on sea walls. There are also circumstances in which the effect of upward impact of a wave beneath a rigid horizontal surface needs to be estimated. This is primarily related to the design of offshore oil rigs in which platform decks may be subject to slamming due to particularly high waves such as freak waves. Experimental work has focused on measurements of wave-induced vertical forces (e.g. Suchithra & Koola 1995). Relatively little theoretical study has been made of the hydrodynamics of upward impact on horizontal surfaces (e.g. Wood & Peregrine 1996).

For industrial applications, the importance of the stability of a vehicle or vessel transporting liquids in partially full tanks has led to the need for understanding the strong and violent liquid motion inside confined spaces (Abramson 1966). We use 'strong' to refer to $O(g)$ water accelerations, 'violent' to accelerations much greater than g. Tank acceleration may give rise to two very different types of responses which often coexist: a violent brief impact of the liquid on the container wall and large-amplitude sloshing motions. Violent impacts induce very large peak pressures which can be analysed by means of the pressure-impulse theory (Cooker & Peregrine 1995; Wood & Peregrine 1996). After the initial stages of liquid acceleration/deceleration a long-lasting sloshing motion induces moderate-to-large pressures on the tank walls. Interaction of lengthwise and spanwise waves generated by periodic and quasi-periodic parametrically forced sloshing in a rectangular channel have been studied experimentally by Underhill, Lichter & Bernoff (1991). Ye & Birk (1994) and Ye (1990) report on very high pressures inside a partially filled tank in the shape of a horizontal circular cylinder. The water motion is forced by an impulse on the end of the tank. Recently Faltinsen *et al.* (2000) investigated the nonlinear sloshing in a rectangular tank using modal analysis and compared results of their model to steady-state solutions and experimental results.

An important characteristic of sloshing motions in a tank is the generation of patterns of steep standing waves. These may be induced by the instabilities of a parametrically driven liquid surface. For example, when a container of liquid is subject to vertical sinusoidal oscillations, the free surface becomes unstable at a critical driving frequency and gives rise to standing waves. These are known as 'Faraday waves' and have been extensively investigated for weak forcing in the last two decades (e.g. the review paper by Miles & Henderson 1990). More recently attention has been paid to understanding the dynamics of steep and breaking Faraday waves. For example Jiang, Perlin & Schutz (1998, hereinafter referred to as J98) describes experiments with sufficiently large forcing for breaking to occur in three recurrent modes. Among these are flat crests which break and which we call a 'table-top' breaking wave ('mode B' of J98). Drop ejection from the crests of waves has been investigated by Goodridge, Hentschel & Lathrop (1999) who derived some statistical characteristics of ejections. Another approach to standing waves is to consider waves reflected at a vertical wall. Such experiments described by Longuet-Higgins & Drazen (2002) also show evidence of a three-period crest variation, with sharp and flat crests.

Since the development of numerical methods to model steep and overturning waves, initially by Longuet-Higgins & Cokelet (1976), there have been a variety of computations of standing waves. Mercer & Roberts (1992, 1994) were the first to accurately model periodic steep two-dimensional standing waves. They also found that very steep standing waves on deep water are typically unstable to subharmonic perturbations via a sideband-type instability. More commonly, initial conditions related to those appropriate for linear standing waves, but with greater energy, have been used to follow the evolution of very steep waves. Most of this work has been reported in conferences, theses, or internal reports, e.g. McIver & Peregrine (1981),

Anderson, Diver & Peregrine (1990) and Topliss (1994). More recently results for such extreme standing waves on deep water have been presented by Longuet-Higgins (2000, 2001) and Longuet-Higgins & Dommermuth (2001*a*, *b*). These computations show energetic events with steep and narrow jets and wider 'table-top' crests. However, a general characterization of these nearly breaking and breaking standing waves has not been developed. Their connection with similar energetic waves in a moving container is only partially described in the literature and development of the connection between experiment and computation is one of the aims of this work.

Experimental observations of sloshing and steep Faraday waves generated in a rectangular tank of dimensions $1480 \times 400 \times 750\,\mathrm{mm}^3$ (length $\times$ width $\times$ height) are reported. The standing waves of the present study are significantly larger than the waves described in J98. The experiments were carried out at the University of Bristol in 1996 and have previously only been described in a very brief internal report (Brocchini, Peregrine & Thais 1997). Unlike most previous studies we do not aim to investigate time-periodic water motion. Although sinusoidal forcing is used, it is sufficiently strong to give rapid growth of waves. In this paper we present results from video recordings that show growth of waves to their maximum steepness. Aspects such as breaking and splashing are left for later study. This limitation is chosen so that we can also present numerical studies of the same motions.

The relatively large scale and short duration of our experiments mean that we can use classical water wave modelling with irrotational flow, neglecting the effects of air, viscosity and surface tension. For such two-dimensional flows in a limited domain the natural approach is to use boundary-integral computational methods. However, we also use an extended set of Boussinesq equations (Wei *et al.* 1995), for three reasons.

(*a*) These, essentially long wave, equations have been extended in recent years to model a wider range of waves and have previously only been compared with travelling waves.

(*b*) Boussinesq equations give much greater scope for numerical modelling of large two-dimensional domains and three-dimensional wave fields. Boundary-integral methods are still too computationally demanding for practical three-dimensional applications.

(*c*) For forcing by horizontal tank motions it is easier for us to model the gentle initial motion with Boussinesq equations than to make the appropriate modifications to our boundary-integral program.

Thus we report comparisons with both Boussinesq and boundary-integral computations that reach the limits of their applicability. Sample boundary-integral computations of features where we could not make direct comparisons with experiment are presented. These are graphical comparisons. We do not attempt careful checks on their 'validity' since for irrotational flow this should be done by comparison with accurate solutions rather than with experiments. We note that Tilman (1993) made an extensive (>500 periods), and successful, comparison for periodic standing waves with essentially the same boundary-integral program as used here.

The experimental setup is described in § 2, and the experimental results are discussed in § 3. The Boussinesq model is developed in § 4. Boundary conditions at the tank walls taking the horizontal acceleration into account are derived, and a test of the model with standing waves (no external forcing) is presented. In § 5 numerical results for the free-surface elevation and pressure are compared to experimental results for an experiment with horizontal shaking. Numerical results for an experiment with vertical shaking are presented in § 6. In this section we also present simulations carried out with a fully nonlinear boundary-integral solver, both as a continuation of the

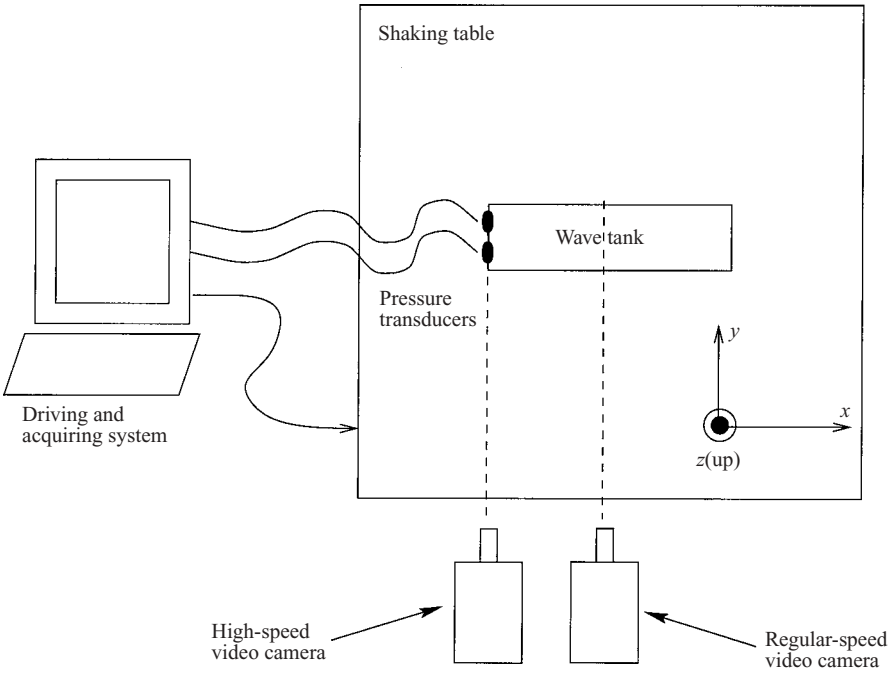

FIGURE 1. Sketch of the experimental setup (top view).

results of the Boussinesq solver and as sample computations for appropriate initial conditions. The continuation from the Boussinesq solver computations compares well with the experimental results. The sample computations show high table-top waves. A discussion of the findings of both experimental and numerical investigations is given in § 7.

2. Experimental setup

In this section a brief overview is given of the equipment and the methodology used during the experimental investigation.

2.1. *The experimental equipment*

In the experiments a rectangular, narrow, glass tank was subjected to either horizontal or vertical motion, by using the Earthquake Shaking Table Facility of the University of Bristol's Civil Engineering Department (figure 1). The shaking table consists of a $3 \times 3\,\mathrm{m}^2$ cast aluminium platform with active control of all six degrees of freedom of motion (i.e. the three translational modes and the roll, pitch and yaw rotational components). In the experiments described here only translational motion, in the vertical and one horizontal direction, was used. A wide range of operational frequencies ($0 < f < 100\,\mathrm{Hz}$) can be used (see e.g. Mir & Taylor 1995).

A glass and steel tank of internal dimensions $1480 \times 400 \times 750\,\mathrm{mm}^3$ (length $\times$ width $\times$ height) was fixed on the shaking table, so that the horizontal shaking was parallel to the long side of the tank (x-direction). The tank was also given vertical shaking (z-direction). We used a sealed tank in order to protect the facility from the water.

The experiments were recorded by two stationary video cameras: one regular-speed camera (25 frames per second) and one high-speed camera (200 frames per second).

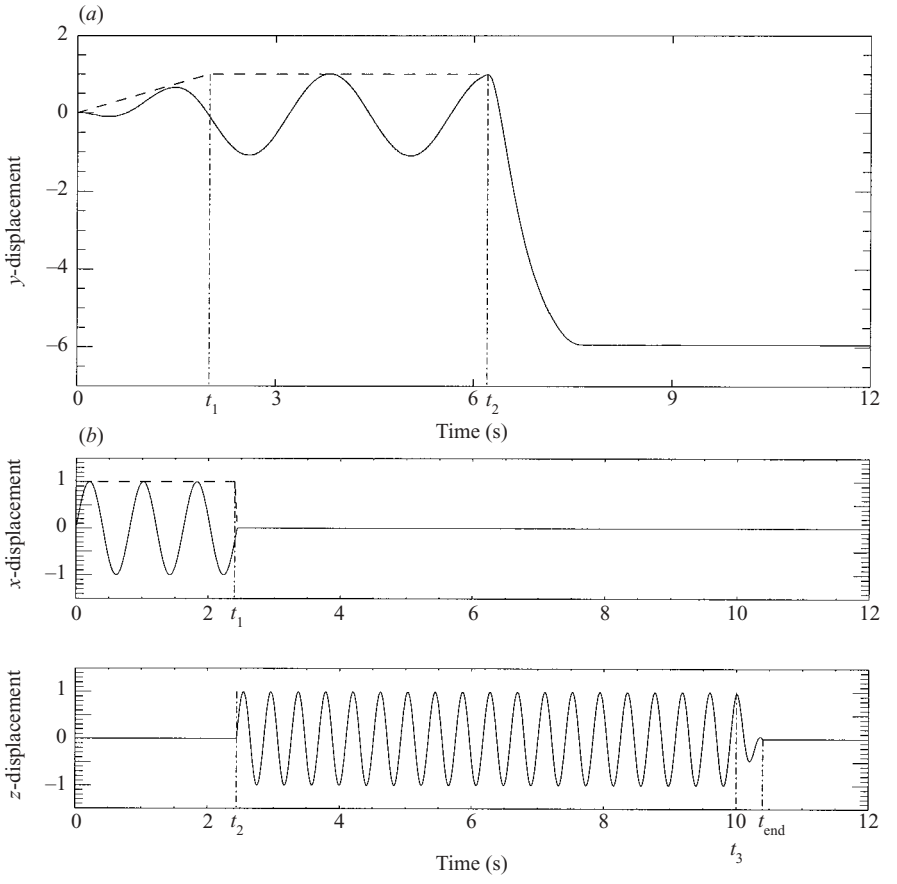

FIGURE 2. Typical examples of the driving signals used in the experiments (normalized). (*a*) Example of a type 'H' signal (experiment H10). (*b*) Example of a type 'V' signal (experiment V21). Their main generation characteristics are reported in table 1.

The latter was used in order to better capture flow features occurring at small time scales at the left-hand tank wall. The cameras were sufficiently far from the tank that lens distortions were negligible. All measurements and comparisons are taken on the front face of the tank. Data were also collected from pressure transducers fitted into the left-hand tank wall, but little of this data proved to be satisfactory. A red LED which switched on at the start of each shaking sequence was fitted at the base of the tank, allowing time synchronization between the regular-speed camera and the data acquiring computer.

2.2. *The driving signals*

Four different signals were created to generate the shaking of the table. Of these only two are reported here. The signals of type 'H' generate horizontal motions and signals of type 'V' drive a horizontal motion followed by a vertical motion. Typical examples are illustrated in figure 2. Table 1 reports characteristics of the driving signals of each type for examples illustrated in this paper. T_{lin} denotes the period of the wave mode excited, which is derived from linear theory as noted below. To obtain the physical displacement of the tank in centimetres, the numbers on the plots should be

Name	h (m)	T_{lin} (s)	t_1 (s)	t_2 (s)	t_3 (s)	t_{end} (s)	Δt	R_{fact}	Scale$_x$	Scale$_z$
H10	0.155	2.443	2.0	6.21	—	—	0.25	−6.0	2.0	—
V05	0.400	0.800	2.0	2.40	8.0	8.4	—	—	0.5	3.0
V11	0.200	0.860	2.5	3.52	10.0	10.4	—	—	1.0	2.0
V21	0.302	0.812	2.4	2.44	10.0	10.4	—	—	1.0	1.0

TABLE 1. Generation characteristics of signals illustrated on figure 2.

multiplied by the scaling factors in the last two columns of the table. On the basis of these model signals, a large number of tests were performed by changing either the still water depth h, or the amplitude of the signal. The different test cases were labelled by the signal type ('H' or 'V') followed by a progressive run number. For example, test H10 is the 10th experiment generated with a signal of type 'H'.

For the experiments involving horizontal shaking only, linear wave modes with half a wavelength in the tank were excited. The shaking frequency was determined as the resonant linear wave frequency for the chosen still water depth and wave mode. Vertically forced standing waves were excited in the mode having three half-wavelengths in the tank. The vertical shaking frequency was twice the linear wave frequency of this mode for the water depth chosen in order to excite parametric resonance (Benjamin & Ursell 1954).

2.2.1. *Signal type 'H': horizontal oscillation plus a push*

In this motion horizontal oscillation in the x-direction was followed, after an interval, by a longer push introduced to enhance wave impact on the endwall of the tank. The amplitude of the sinusoidal motion builds up from zero to one, reached at time t_1. At time t_2 the tank is moved to the position R_{fact} in an exponentially decaying motion of time scale Δt. The tank motion effectively stops, and if the timing is appropriate, a violent wave impact may occur on the wall in a fixed tank. Figure 2(a) shows the specific driving used for test H10 (normalized) as an example of a type 'H' signal.

2.2.2. *Signal type 'V': horizontal then vertical oscillation*

This signal was designed to generate standing waves forced by vertical oscillation. It generates a mixed horizontal and vertical motion. The wave tank is initially oscillated horizontally a few times and, subsequently, oscillated in the vertical direction. This mixed signal is useful, as the initial still water condition is not suitable for obtaining deterministic Faraday waves. The initial horizontal motion is used to produce a small perturbation to the flat still water surface that provides the 'seed' for amplification by the vertical forcing. An example of the driving signals is given on figure 2(b), where the normalized displacements in both x- and z-directions are shown for experiment V21. Horizontal oscillation is kept constant until time t_1, then its amplitude is decreased linearly to zero at time t_2 when the vertical motion is impulsively started. This motion is then linearly reduced to a zero amplitude in the time span $t_3 < t < t_{\text{end}}$. After this time the waves evolve in a stationary tank. Note that the forcing frequency is doubled for the vertical motion. The forcing in these examples is strong. Its simplest measure is the maximum acceleration input through the driving signal:

$$\text{e.g. V05: } 0.75g.\ \text{V11: } 0.44g.\ \text{V21: } 0.24g.$$

The measured accelerations were slightly lower, see for example figure 14.

3. A qualitative analysis of experimental observations

The discussion of the experimental observations is based upon a few specific tests which highlight characteristic flow features. We divide the discussion into horizontally and vertically driven shaking, since the typical manifestations differ accordingly.

3.1. *Horizontal shaking*

For the horizontal test cases we used the high-speed video camera in conjunction with the regular-speed video camera to visualize any rapid surface motions which occur on time scales of some milliseconds. For test H10 which is reported here, the still water depth in the tank was $h = 155$ mm. The relatively low water depth is crucial for obtaining clean visual recordings: no water sheets reach the lid of the tank and no spray and droplets are generated which could disturb the free water surface. The initial low-amplitude sloshing soon developed into a solitary wave propagating back and forth, agreeing with the observations of Chester & Bones (1968) and hence not detailed here.

Figure 3 shows a sequence of snapshots taken by the regular-speed video camera to show the interaction of a steep wave with the left-hand sidewall of the tank. During the impact with the wall a thin sheet of water is generated and pushed upwards by the wave. In these conditions features of the interaction of the water with the tank walls are best captured by the high-speed video camera, and are shown in figure 4. The wave behaviour is similar for other cases, such as for the same wave when after reflection it meets the right-hand wall.

As may be seen in both figures 3 and 4, the wave drives a thin sheet of fluid up the wall. The bulk of the wave is reflected before the sheet descends and the crest moves away from the wall. The jet is then in free fall, and is entirely independent of the wave that generated it. As it accelerates downward it forms a depression on the surface. With jets that reach as high as those in these experiments, the depression becomes so deep that a considerable amount of air is entrained. The water initially displaced by the falling jet then falls back towards the wall trapping more air and at the same time forming a small short second reflected wave. An almost identical sequence is seen later when the almost-solitary wave reaches the right-hand wall. A similar depression formed at the end of a falling jet from a 'free' crest may also be seen in frame 14 of figure 5 at $t = 5.36$ s.

This behaviour of the falling jet is virtually identical to the impact of a finite falling jet in the absence of a wave, which is well-documented by experiment and computations in Zhu, Oguz & Prosperetti (2000). There is also some similarity with air entrainment by steady two-dimensional (Cummings & Chanson 1999) and three-dimensional jets (Ervine & Falvey 1987). The same type of motion modelled numerically from 'standing wave' initial conditions is described well in Longuet-Higgins (2000, 2001) and Longuet-Higgins & Dommermuth (2001*a*, *b*).

3.2. *Vertical forcing*

The most interesting free-surface features of steep standing waves generated by vertical oscillations of the tank are modes of incipient breaking. The visual analysis relies only on regular-speed video camera images, as there is no special need for resolution at higher frequencies.

Figure 5 shows a sequence of video snapshots for the test case V05. The sequence shows the generation of sharp-crested waves followed by flat-topped waves. Times for each snapshot are given in the upper right corner of each frame. For this case the

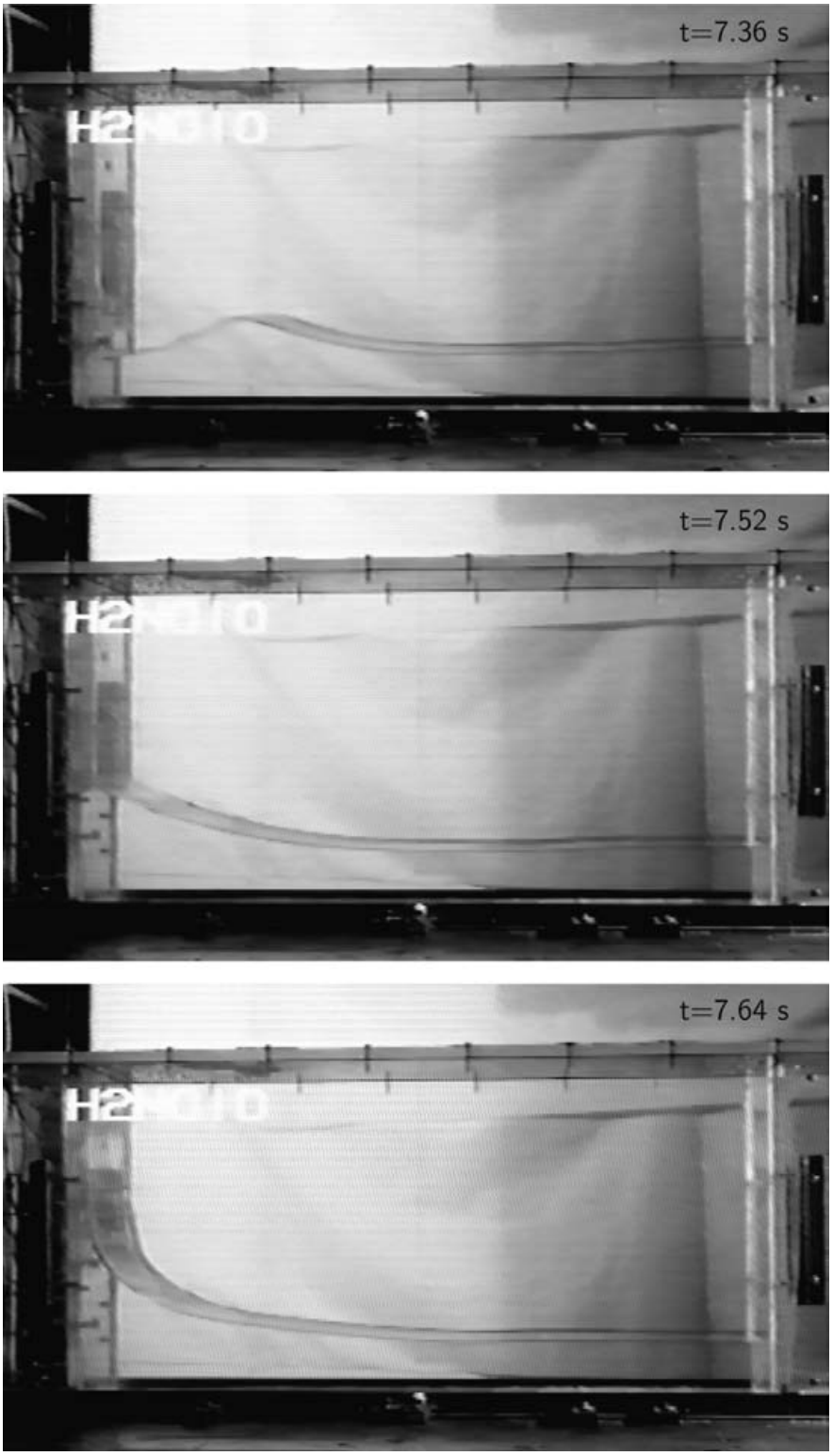

FIGURE 3. Horizontal oscillation. Sequence of snapshots taken by a regular-speed video camera (25 frames per second). Test case H10.

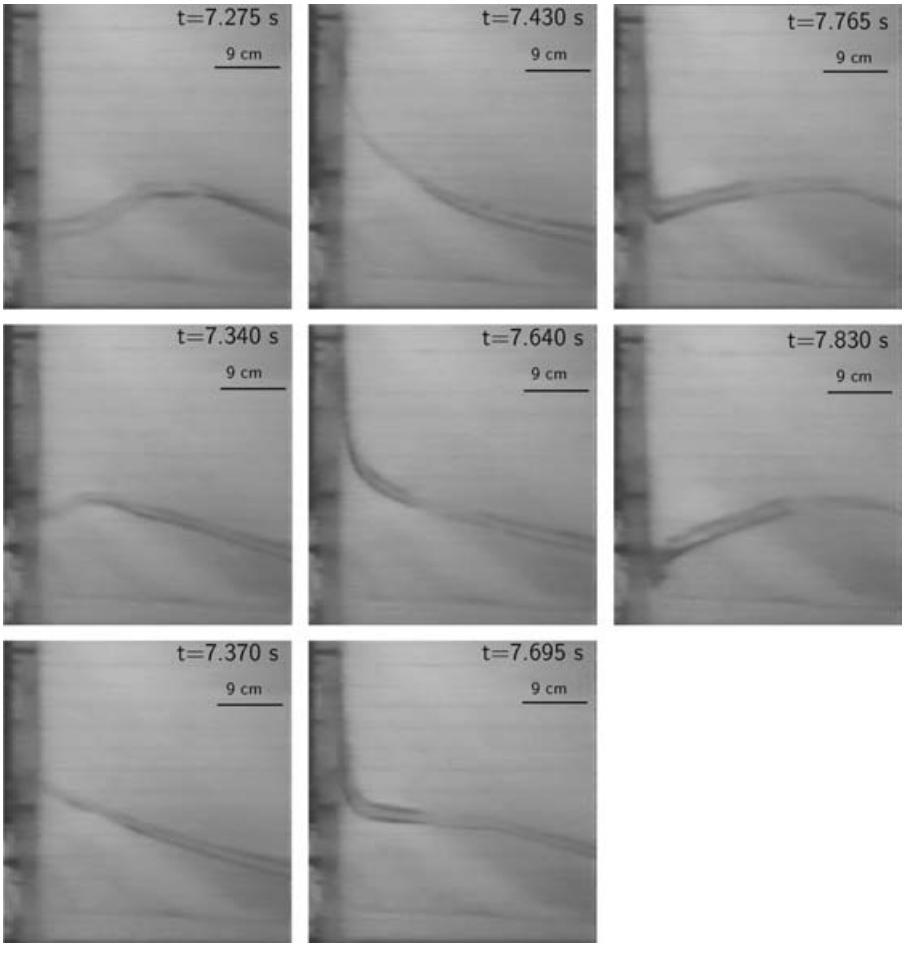

FIGURE 4. Horizontal oscillation. Test case H10 (same as in figure 3). From top to bottom and from left to right a time sequence of snapshots taken by a high-speed video camera (200 frames per second).

still water depth in the tank was $h = 400$ mm. The process of steepening of successive wave crests can be observed by comparing the first two frames of figure 5.

Although the sharp crest in frame 2 of figure 5 is very steep, and appears to retain its identity as it falls through to frame 5, it does not form any localized depression, although it trails a very thin sheet of water that breaks up into drops. However, the next crest to rise is more energetic, and although slightly modified by touching the top of the tank, frame 14 ($t = 5.36$ s) shows that at the end of its fall a depression is created.

Frames 7 and 8 of figure 5 ($t = 5.04$ s and 5.12 s) show the early stages of what is becoming a flat-topped crest. The evolution of the flat-topped crest, which we refer to as a 'table-top' shape, is seen in the final eight frames of figure 5, where the process is illustrated frame by frame. The 'table top' we see here is associated with a much more energetic free-surface motion than any of the 'mode B' breakers reported by J98. The flat-topped shape is developed early in the upward motion and on the twelfth frame of figure 5 at $t = 5.28$ s, the crest sides are almost vertical below the really flat top (hence the name 'table top'). The final four frames show the transition from upward to downward motion. Careful examination of the video shows that this crest

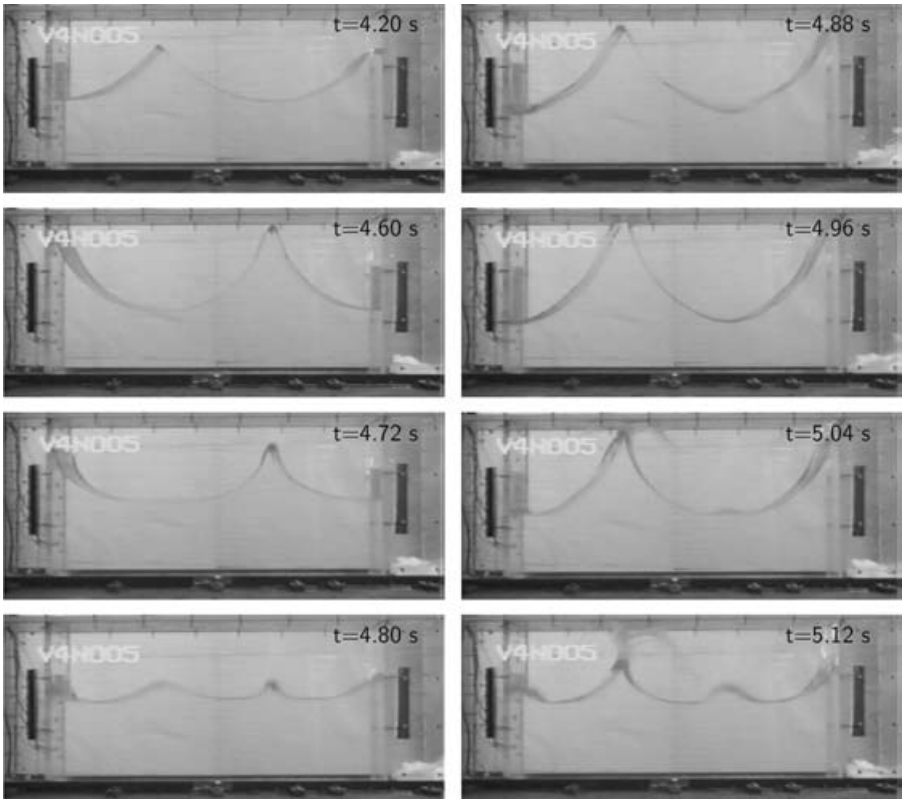

FIGURE 5. See facing page for caption.

just misses touching the top of the tank, whereas the other flat-topped crest, moving up and down the left-hand wall, does just touch the top. We here observe that the distance between the sides decreases slightly, thus resulting in a slight 'thinning' of the wave profile. The thinning is quantified by measuring the thinnest width of the profiles for $t = 5.28$ s and $t = 5.44$ s. The widths measured are marked by horizontal lines on the images and we find that the width reduces by 12% between the two instants. Thinning of both sharp and flat-topped crests is common in our experiments and justifies further investigations.

The surface of the 'table-top' wave is roughened from its inception since the previous pair of sharp crests touch the roof (figure 5 frames 6 and 7) and water drops land on this, the next crest to rise. It is noticeable that the roughness increases as the crest nears its maximum elevation and then starts to fall. This increased roughness is explained by considering figure 6. The displacement of the top of the crest is plotted against time, and compared with a parabola, which would be obtained for a particle in free fall. The result shows that a large portion of the crest motion is very close to free fall for the time period from 5.12 s to 5.56 s as labelled in figure 5. This is almost a whole period of the forcing (half the period of the excited wave). Thus if there is any disturbance on the surface there is almost no restraint on its growth, should any portion of the surface have velocities moving away from the bulk of the fluid. Hence it is particularly easy for drops to form. While a free fall behaviour is expected close to the instant of maximum crest elevation, the proximity to free fall for almost all of the table-top crest's evolution is remarkable.

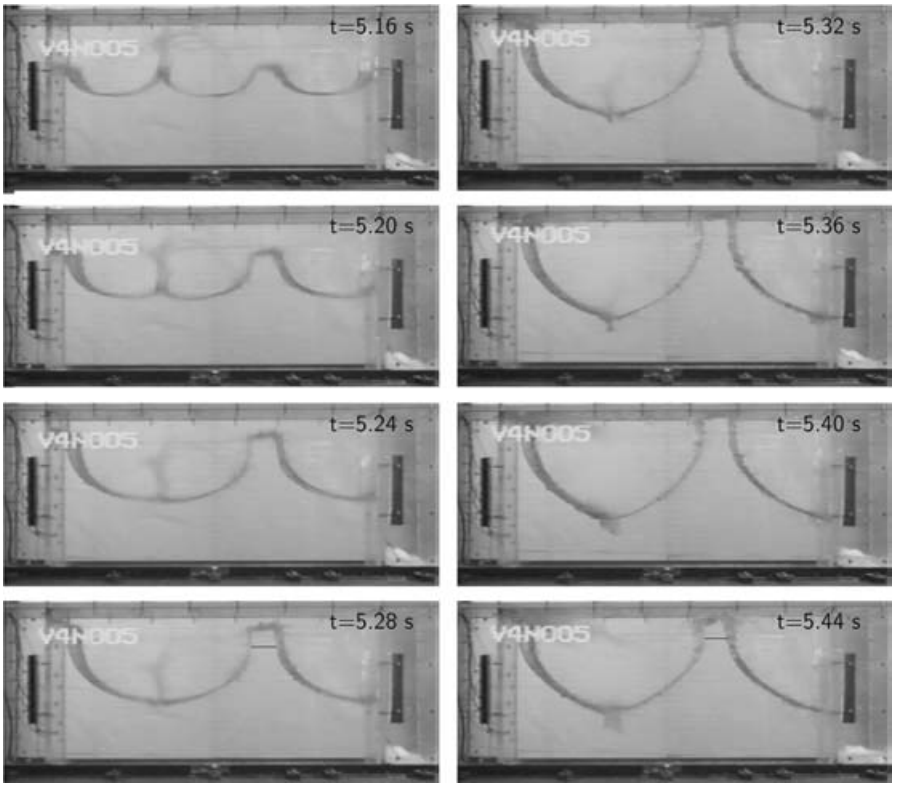

FIGURE 5. Vertical shaking. From top to bottom and from left to right a time sequence of snapshots taken by a regular-speed video camera (25 frames per second). Test case V05.

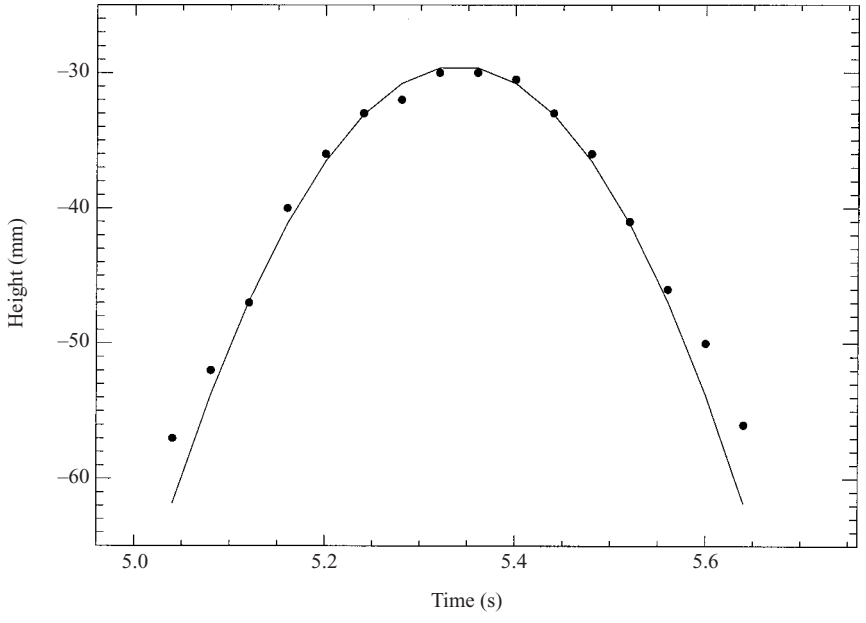

FIGURE 6. Crest elevation for the 'table-top' wave of figure 5 compared to a free fall parabola (continuous line). Points are measured from the top of the video frame (to an accuracy of roughly 0.5 mm), and hence refer to a stationary frame of reference.

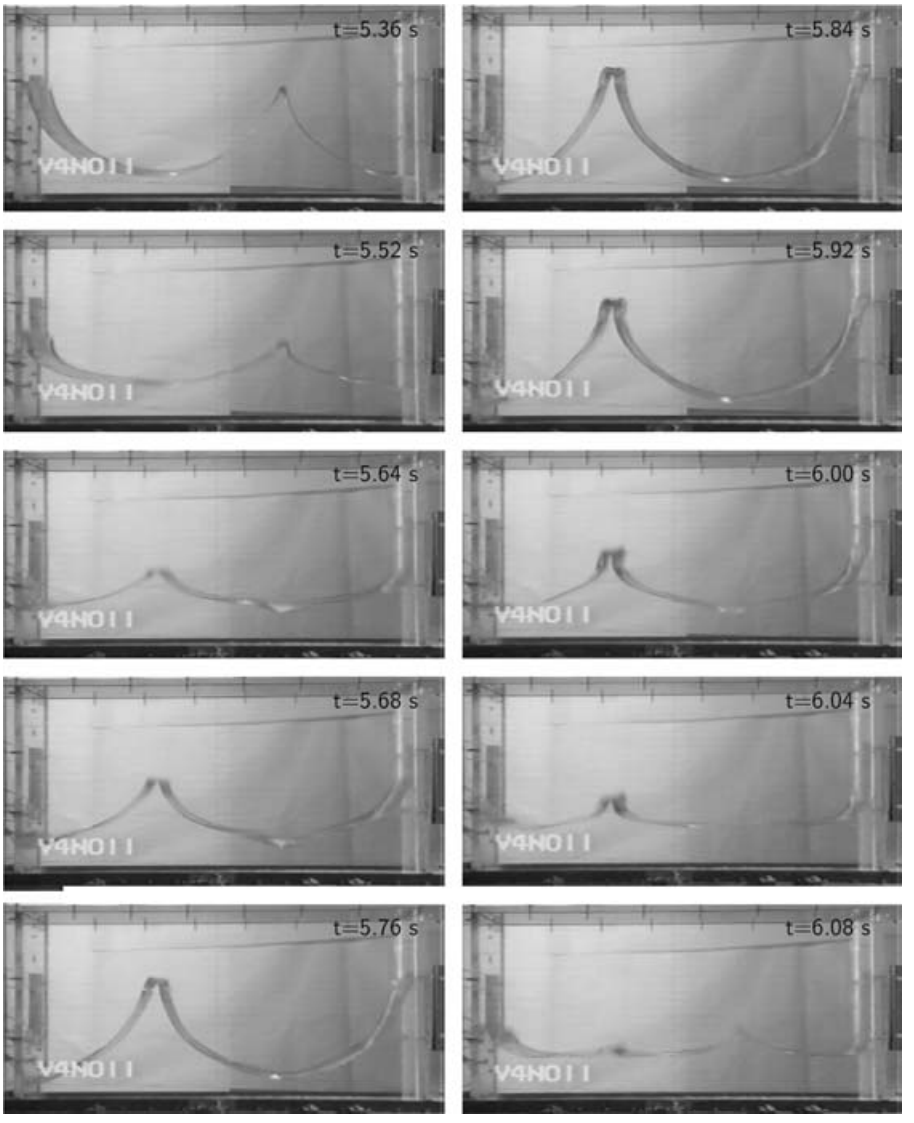

FIGURE 7. Vertical shaking, test case V11. From top to bottom and from left to right a time sequence of snapshots taken by a regular-speed video camera (25 frames per second).

Figure 7 illustrates the evolution of a 'table top' for the test case V11 similar to that of figure 5. In this case there is a lower initial still water depth of $h = 200$ mm and there are few disturbances due to previous fragmentation into water drops. The downward motion of the wave is characterized by retaining the square shape of the crest with almost vertical sides. In this case there continues to be less surface disturbance and thinning of the crest is only observable in the last frames of the figure. Perhaps more significantly this is a thinner crest than that illustrated in figure 5, and in frames 6 and 7 it is not so very different from the 'type A' crest of J98. This variation in width of table-top crests demonstrates that there is almost certainly a continuum of shapes between sharp crests and table-top crests. Unlike J98 where a three-fold periodic variation of crest types was observed we see no systematic variation, except that the first table-top crest always followed a steep sharp crest.

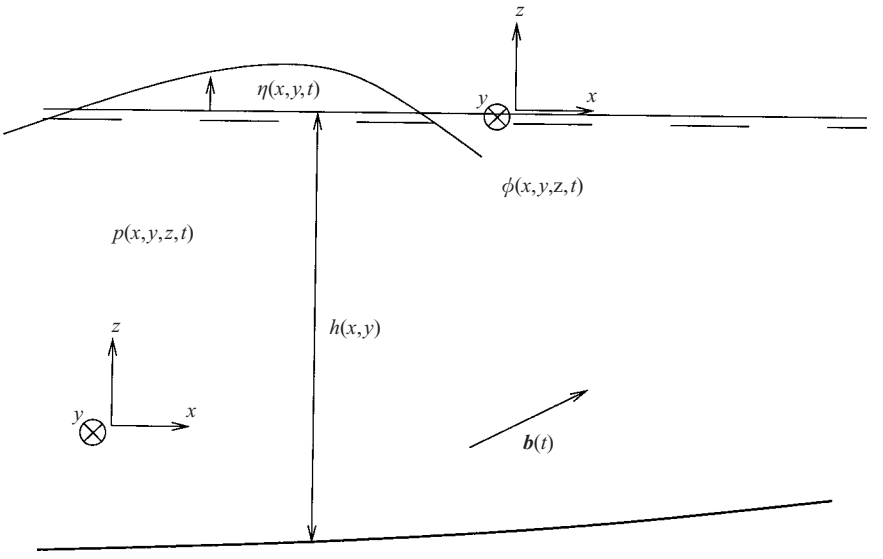

FIGURE 8. Definition sketch for a fluid domain subject to an external acceleration $\boldsymbol{b}$.

In all the experiments we could see no sign of three-dimensional motion until the surface commenced to break into droplets. Sometimes this was more pronounced, or started first, near the walls.

4. A Boussinesq-type model for forced waves

In the following we present a modified Boussinesq-type model, capable of simulating much of the wave motion in the accelerated tank.

Boussinesq models are depth-integrated models describing the inviscid flow of an incompressible fluid with a free surface. They can be obtained by asymptotic expansions from the shallow-water limit by assuming $O(\mu^2) = O(\delta) \ll 1$ (e.g. Mei 1983). Here $\mu = 2\pi h_0/L_0$ and $\delta = a_0/h_0$ are parameters which give a measure of the dispersive and nonlinear effects respectively, with h_0, L_0 and a_0 being a typical water depth, wave length scale and wave amplitude, respectively.

A number of modified Boussinesq models have been proposed in recent years, with continuously improving linear dispersion and shoaling characteristics along with other measures of the accuracy of the equations, see the review paper of Madsen & Schäffer (1999) and also Gobbi, Kirby & Wei (2000) and Madsen, Bingham & Liu (2002*a*). In the present study, we use the model of Wei *et al.* (1995), derived by assuming $\delta = O(1)$, retaining all powers of δ within the $O(\mu^2)$-expansion. Thus for long enough waves, the model takes full account of the nonlinearity.

4.1. *Extension of the model to incorporate external acceleration*

The forced waves are modelled in the non-inertial frame of reference which follows the tank motion. This simplifies the modelling, since no moving boundaries have to be considered. The movement of the tank, however, imposes additional apparent body forces in the fluid domain, and we therefore need to modify the Boussinesq model to take the acceleration into account.

We consider an infinitesimal element of fluid, subject to an external acceleration $\boldsymbol{b} = (b_1, b_2, b_3)$, see figure 8. The acceleration is allowed to vary in time, $\boldsymbol{b} = \boldsymbol{b}(t)$.

A Cartesian coordinate system (x, y, z) is introduced, with the z-axis pointing upwards from the still water level. The fluid velocity components are denoted $\boldsymbol{u} = (u, v, w)$, the density and the pressure ρ and p respectively. We assume that the fluid is incompressible and neglect any effects of viscosity, surface tension and turbulence. Momentum conservation for an infinitesimal element of fluid gives the Euler equation of motion:

$$\boldsymbol{u}_t + (\boldsymbol{u}\cdot\nabla)\boldsymbol{u} = -\frac{\nabla p}{\rho} + \boldsymbol{b}(t). \tag{4.1}$$

Taking the curl of this equation gives the transport equation for vorticity $(\boldsymbol{\omega} = \nabla \times \boldsymbol{u})$, which for a fluid element can be written as $\mathrm{D}\boldsymbol{\omega}/\mathrm{D}t = (\boldsymbol{\omega}\cdot\nabla)\boldsymbol{u}$. Since we impose no angular motion on the tank, the external forcing $\boldsymbol{b}(t)$ is uniform in space and does not alter this result. Thus, since the vorticity is zero when the fluid is at rest, the flow continues to be irrotational as long as the free surface remains simply connected. Hence we may introduce a velocity potential $\phi(\boldsymbol{x}, t)$ such that $\boldsymbol{u} = \nabla\phi$. On substituting ϕ into (4.1) and integrating once in space, we obtain

$$\phi_t + \tfrac{1}{2}(\nabla\phi)^2 = -\frac{p}{\rho} + \boldsymbol{b}(t)\cdot\boldsymbol{x} + C(t), \tag{4.2}$$

where $\boldsymbol{x} = (x, y, z)$ and $C(t)$ is an arbitrary function of time. We absorb this function in the potential itself, since a time-dependent part of the potential does not change the fluid velocities $\boldsymbol{u} = \nabla\phi$. For $\boldsymbol{b} = (0, 0, -g)$, equation (4.2) simplifies to give the usual Bernoulli equation.

We now change the notation such that $\nabla = (\partial/\partial x, \partial/\partial y)$ and $\boldsymbol{u} = (u, v)$, so that the equations governing the fluid motion are,

$$\nabla^2\phi + \phi_{zz} = 0, \quad -h \leqslant z \leqslant \eta, \tag{4.3}$$

$$\nabla\phi\cdot\nabla h + \phi_z = 0, \quad z = -h, \tag{4.4}$$

$$\phi_t - \boldsymbol{b}\cdot(x, y, \eta) + \tfrac{1}{2}\left[(\nabla\phi)^2 + \phi_z^2\right] = 0, \quad z = \eta, \tag{4.5}$$

$$\eta_t + \nabla\phi\cdot\nabla\eta - \phi_z = 0, \quad z = \eta, \tag{4.6}$$

describing the incompressibility of the flow, (4.3), and the impermeability of the bottom and the free surface (4.4), (4.6). The dynamic free-surface boundary condition, (4.5), formed from (4.2), imposes constant pressure at the free surface, chosen to be zero, as the reference pressure. For $\boldsymbol{b}(t) = (0, 0, -g)$ these four equations are the basis for the derivation of the model of Wei *et al.* (1995). Note that the external acceleration $\boldsymbol{b}(t)$ only alters (4.5).

The equations of Wei *et al.* (1995) are derived by using an expansion of the velocity potential from an arbitrary reference level $z = \hat{z}(x, y)$. The expansion can be achieved by first expanding from the bottom, utilizing the Laplace equation and the bottom boundary condition

$$\phi = [\phi]_{z=-h} - (z+h)\nabla h\cdot[\nabla\phi]_{z=-h} - \tfrac{1}{2}(z+h)^2[\nabla^2\phi]_{z=-h} + O(\mu^4). \tag{4.7}$$

Evaluating this equation at $z = \hat{z}$ and subtracting the result obtained from (4.7) yields a relation between ϕ and $\hat{\phi} \equiv [\phi]_{z=\hat{z}}$, involving gradients of the potential at the bottom. Within the μ^2-expansion, these gradients, however, can be consistently replaced by the same gradients evaluated at an arbitrary z-level. Choosing this level to be $\hat{z}$, the expansion

$$\phi = \hat{\phi} + (\hat{z} - z)\nabla\cdot(h\nabla\hat{\phi}) + \tfrac{1}{2}(\hat{z}^2 - z^2)\nabla^2\hat{\phi} + O(\mu^4), \tag{4.8}$$

is obtained. This expansion is used later to derive an expression for the fluid velocities and pressure within the fluid.

With the modified dynamic free-surface boundary condition, (4.5), the derivation of Wei *et al.* (1995) is easily adapted for the case of accelerated motion. In the case of only one horizontal dimension and constant depth the resulting equations are

$$\eta_t + h\hat{u}_x + (\eta\hat{u})_x + \left(\alpha + \tfrac{1}{3}\right)h^3\hat{u}_{xxx} + \alpha h^2(\eta\hat{u}_{xx})_x - \tfrac{1}{2}h(\eta^2\hat{u}_{xx})_x - \tfrac{1}{6}(\eta^3\hat{u}_{xx})_x = O(\mu^4), \quad (4.9)$$

$$\hat{u}_t - b_1 - b_3\eta_x + \hat{u}\hat{u}_x + \alpha h^2\hat{u}_{xxt} - \left[\left(h + \tfrac{1}{2}\eta\right)\eta\hat{u}_{xt}\right]_x + \left[\alpha h^2\hat{u}\hat{u}_{xx} - \left(h + \tfrac{1}{2}\eta\right)\eta\hat{u}\hat{u}_{xx}\right]_x + \tfrac{1}{2}\left[\left(h + \eta\right)^2\hat{u}_x^2\right]_x = O(\mu^4). \quad (4.10)$$

Here, the velocity variable adopted, $\hat{u}$, is the horizontal velocity at $z = \hat{z}$ and the dimensionless parameter α is defined as

$$\alpha = \frac{\hat{z}}{h} + \frac{1}{2}\left(\frac{\hat{z}}{h}\right)^2. \quad (4.11)$$

The choice of α governs the linear dispersion characteristics of the equations. For $\alpha = -2/5$, the squared dimensionless linear phase speed of the equations is the Padé [2,2] approximant of the similar result for fully dispersive theory. In the present work, however, we use the value $\alpha = -0.39$ as suggested by Nwogu (1993) to optimize the phase velocity of linear waves. Note, for examples where h is a function of $\boldsymbol{x}$ this means that $\hat{\boldsymbol{z}}$ is also a function of $\boldsymbol{x}$: we allow for this more general case in the following analysis.

For an infinitesimal column of water stretching from the bottom to the free surface, (4.9) and (4.10) state conservation of mass and momentum, respectively. Conservation of mass is unaffected by the external acceleration, and therefore the new terms due to the external forcing only enter the momentum equation. For $\boldsymbol{b} = (0, 0, -g)$ the model simplifies to the one-dimensional constant-depth version of the model of Wei *et al.* (1995).

4.2. *Boundary conditions at the tank walls*

In this study viscous effects are neglected, so we do not consider any boundary layer effects at the walls, and we consider only two-dimensional, (x, z), motions. At the scale of our experiments, we do not expect surface tension to be important, except at the sharpest crests, and as in equations (4.9) and (4.10), we do not include surface tension in the boundary conditions. The vertical forcing frequencies were chosen so that we could compare motion at a sidewall with motion two thirds of the tank length away from the wall. For ideal inviscid flow with no surface tension effects there should be no difference. In the motion that develops before substantial splashing takes place, figure 5 shows the largest discrepancies we have seen. Frames 7 and 8 of figure 5 show that the free crest touches the tank roof whereas the crest at the wall does not. On the other hand, the converse is true for the next crest to arise, see the last frame of figure 5. Since different sidewalls are involved in these two cases, it is difficult to make any general statement other than that the effects of surface tension and boundary layers are slight.

In the moving reference frame the endwalls of the tank are stationary, thus $u = 0$ at the walls. Laplace's equation for the potential implies

$$u_{xx} = -u_{zz}, \quad (4.12)$$

and at the vertical walls $u=0$ for all z. Thus (4.12) gives $u_{zz}=0=u_{xx}$ at the walls, and thus since these apply for all time we can use

$$\hat{u}=\hat{u}_{xx}=\hat{u}_t=\hat{u}_{xxt}=0, \tag{4.13}$$

at the tank walls.

While the above boundary conditions for the velocity are identical to the unaccelerated case, the usual zero-slope condition for the free-surface elevation at vertical walls does not apply when external acceleration is present. An appropriate boundary condition for η_x can be found by considering the momentum balance at the wall. We apply equation (4.10) at the wall and use boundary conditions (4.13) to obtain an equation which can be solved for η_x. The result is

$$\eta_x=\frac{b_1}{-b_3+(h+\eta)\left(\hat{u}_x^2-\hat{u}_{xt}\right)}+O(\mu^4), \tag{4.14}$$

which together with the above consequences of $u=0$ defines the boundary conditions used.

4.3. *The numerical scheme*

Equations (4.9) and (4.10) with boundary conditions (4.13) and (4.14) are solved using the numerical scheme of Wei *et al.* (1995), first presented in Wei & Kirby (1995). The spatial derivatives are expressed by finite-difference approximations on a uniform grid, providing fourth-order accuracy for the non-dispersive terms. The time-integration is performed using a fourth-order Adams–Bashforth–Moulton predictor–corrector scheme. The boundary conditions are treated by the use of two additional ghost points on the outer side of the tank walls. In order to avoid high-frequency numerical instabilities which occurred for steep wave motion or strong forcing, a five-point smoothing filter was applied when required. This and other smoothing filters are described in Longuet-Higgins & Cokelet (1976) and Dold (1992).

4.4. *Fluid velocity and pressure*

The velocity field and pressure within the fluid can be reconstructed from the velocity variable $\hat{\boldsymbol{u}}$ and η. The fluid velocity at the free surface is needed to transform a solution from the Boussinesq solver to the irrotational flow solver (see § 6.3), while we derive an expression for the pressure to be able to compare numerical and experimental pressure results in § 5.

The horizontal fluid velocity is obtained by calculating $\nabla\phi$ from (4.8):

$$\begin{aligned}\nabla\phi=\nabla\hat{\phi}+\nabla\hat{z}\nabla\cdot(h\nabla\hat{\phi})+\hat{z}\nabla\hat{z}\nabla^2\hat{\phi}\\ +(\hat{z}-z)\nabla\nabla\cdot(h\nabla\hat{\phi})+\tfrac{1}{2}(\hat{z}^2-z^2)\nabla\nabla^2\hat{\phi}+O(\mu^4).\end{aligned} \tag{4.15}$$

We evaluate this at $z=\hat{z}$ to obtain a relation between $\nabla\hat{\phi}$ and $\hat{\boldsymbol{u}}$:

$$[\nabla\phi]_{z=\hat{z}}=\hat{\boldsymbol{u}}=\nabla\hat{\phi}+\nabla\hat{z}\nabla\cdot(h\nabla\hat{\phi})+\hat{z}\nabla\hat{z}\nabla^2\hat{\phi}+O(\mu^4). \tag{4.16}$$

The last two terms on the right-hand side are of magnitude $O(\mu^2)$, thus giving the relation $\nabla\hat{\phi}=\hat{\boldsymbol{u}}+O(\mu^2)$. Hence, $\nabla\hat{\phi}$ can be replaced by $\hat{\boldsymbol{u}}$ in all the terms of $O(\mu^2)$ within the accuracy of the model derivation. Substitution of (4.16) in (4.15) yields

$$\boldsymbol{u}=\hat{\boldsymbol{u}}+(\hat{z}-z)\nabla\nabla\cdot(h\hat{\boldsymbol{u}})+\tfrac{1}{2}(\hat{z}^2-z^2)\nabla\nabla\cdot\hat{\boldsymbol{u}}+O(\mu^4). \tag{4.17}$$

The vertical velocity is found by calculating the z-derivative of (4.8) to be

$$w = -\nabla\cdot(h\hat{\boldsymbol{u}}) - z\nabla\cdot\hat{\boldsymbol{u}} + O(\mu^4). \tag{4.18}$$

The pressure within the fluid can be derived from the modified Bernoulli equation (4.2) which, after absorbing $C(t)$ in the velocity potential, gives

$$\phi_t + \frac{p}{\rho} - \boldsymbol{b}\cdot\boldsymbol{x} + \tfrac{1}{2}\left[(\nabla\phi)^2 + \phi_z^2\right] = 0. \tag{4.19}$$

This is evaluated at $z=\eta$ and subtracted from (4.19) to give

$$\frac{p}{\rho} = -b_3(\eta - z) + (\tilde{\phi}_t - \phi_t) + \tfrac{1}{2}\left((\nabla\tilde{\phi})^2 - (\nabla\phi)^2 + \tilde{\phi}_z{}^2 - \phi_z^2\right), \tag{4.20}$$

where the tilde indicates values at the free surface for the same values of (x, y, t). Substitution of (4.8), (4.17) and (4.18) into the above equation yields

$$\begin{aligned}\frac{p}{\rho} = &-b_3(\eta - z) - (\eta - z)\left[\nabla\cdot(h\hat{\boldsymbol{u}}_t) + (\hat{\boldsymbol{u}}\cdot\nabla)\nabla\cdot(h\hat{\boldsymbol{u}}) - (\nabla\cdot\hat{\boldsymbol{u}})\nabla\cdot(h\hat{\boldsymbol{u}})\right]\\ &- \tfrac{1}{2}(\eta^2 - z^2)\left[\nabla\cdot\hat{\boldsymbol{u}}_t + (\hat{\boldsymbol{u}}\cdot\nabla)(\nabla\cdot\hat{\boldsymbol{u}}) - (\nabla\cdot\hat{\boldsymbol{u}})^2\right] + O(\mu^4),\end{aligned} \tag{4.21}$$

where, again we have used $\nabla\hat{\phi} = \hat{\boldsymbol{u}} + O(\mu^2)$. For one horizontal dimension and uniform depth (4.17), (4.18) and (4.21) reduce to

$$u = \hat{u} + \left[(\hat{z} - z)h + \tfrac{1}{2}(\hat{z}^2 - z^2)\right]\hat{u}_{xx} + O(\mu^4), \tag{4.22}$$

$$w = -(z + h)\hat{u}_x + O(\mu^4), \tag{4.23}$$

$$\frac{p}{\rho} = -b_3(\eta - z) - \left((\eta - z)h + \tfrac{1}{2}(\eta^2 - z^2)\right)\left(\hat{u}_{xt} + \hat{u}\hat{u}_{xx} - \hat{u}_x^2\right) + O(\mu^4). \tag{4.24}$$

4.5. *A test on standing waves*

As a first test of the model's ability to adequately represent steep standing waves we made a simulation using accurate periodic standing wave data from D. H. Smith and A. J. Roberts (1995, private communication) for the initial condition. The method of producing these data is described in Mercer & Roberts (1992, 1994).

The standing wave profile used in the present test is calculated for a dimensionless wavelength of $L/h = 2\pi/0.799$. The wave height is $(\eta_{\max} - \eta_{\min})/h = 0.525$ and the maximum crest acceleration is $w_t/g = -0.30$. The above mentioned smoothing procedure was applied once in each period to prevent the growth of numerical instabilities.

In each cycle, the profile having the deepest trough, and hence negligible fluid velocity, was captured and the error measure

$$\Delta\eta = \frac{\sum_{i=1}^{N} |\eta_i - \eta_{\text{initial},i}|}{\sum_{i=1}^{N} |\eta_{\text{initial},i}|} \tag{4.25}$$

was calculated. When using 81 inner points in the computational domain and a time step of $\Delta t = 1.12\times10^{-2}(h/g)^{1/2}$, this error was found to oscillate around a mean value of 1.04×10^{-2}, as depicted in figure 9. This is an acceptable error and we explain the deviation from the more accurate initial data by the absence of the $O(\mu^4)$-terms in the model. For the present test we have $\mu = kh = 0.799$, and therefore $\mu^4 \sim 0.4$, which cannot be considered small. The envelope of the peaks in the error curve indicates

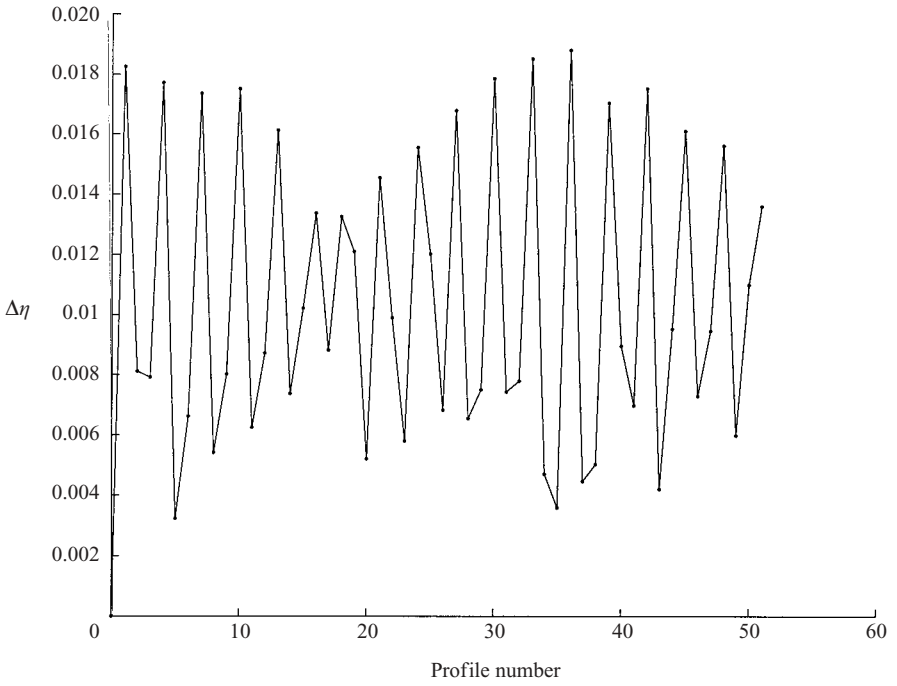

FIGURE 9. Difference between successive extreme standing wave profiles of the deepest trough and accurate initial data. Points are plotted once per period so the connecting lines only show the succession of points.

that a small modulation of the signal is present in the calculations. This is to be expected, since the amplitudes of the higher bound harmonics of the fully nonlinear standing wave profile used as initial condition do not match the amplitudes for a stationary standing wave solution of the present wave model. Again, this is due to the absent terms of $O(\mu^4)$.

5. Numerical results for horizontal shaking

In the following we present typical numerical results for horizontally accelerated flows. The results are generated for the experiment labelled H10. The numerically calculated free-surface profiles are compared with experimental data and an example of a comparison between a measured and a computed pressure time series is also presented.

5.1. *Acceleration of the tank*

For experiment H10, the driving signal is of type 'H' (see figure 2). The measured acceleration of the tank is shown in figure 10. The acceleration was sampled 1000 times per second, but due to substantial noise in the signal measured, the present curve is drawn by averaging the signal over a 200-point moving window.

To simulate the experiment, a signal modelling the acceleration of the tank was constructed. Since the signal refers to the non-inertial moving frame of reference, it has the opposite sign to the measured acceleration. Both the measured and numerically imposed acceleration are shown in figure 10. The sinusoidal acceleration builds up in the time interval $t = [0; 2]$ s and subsequently becomes sinusoidal with a constant

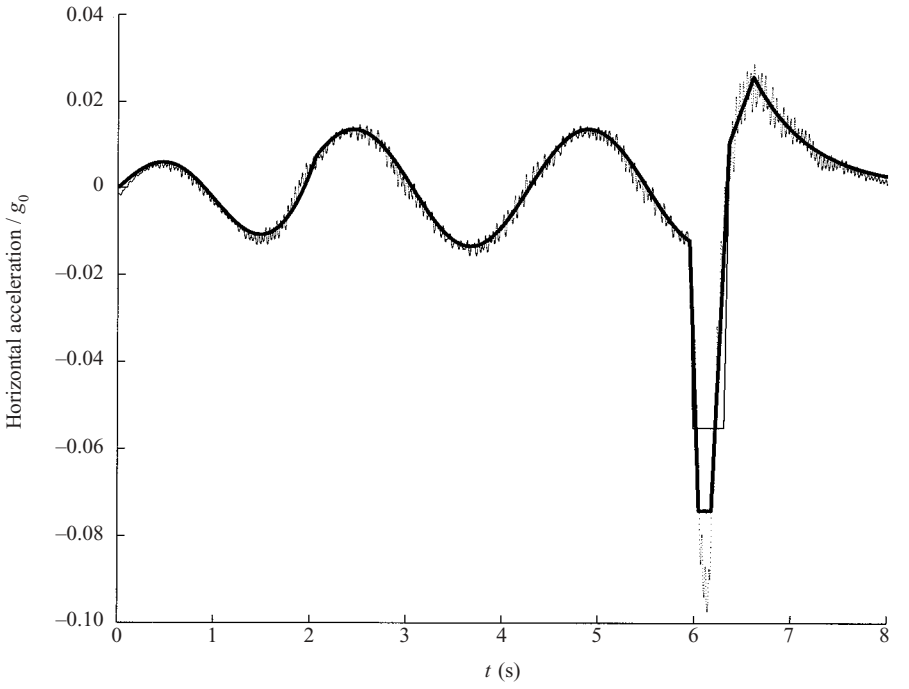

FIGURE 10. Horizontal tank acceleration for experiment H10: ···, measured; ——, modelling signal; ——, alternative modelling signal. Modelling signals are multiplied by (−1).

amplitude. At $t = 5.9$ s the tank is pushed violently towards the left. This results in the negative peak in the measured acceleration, immediately followed by positive acceleration.

In the Boussinesq model, a model signal similar to the data shown was tried. However, the strong accelerations related to the peak gave convergence problems for the corrector scheme at the violent impact at the wall. Hence, a modified signal with a broader representation of the peak for $t = [5.90; 6.60]$ s was used, see figure 10.

The impact on the tank velocity of the acceleration peak and the deceleration is estimated from the data to be

$$\Delta V_1 = \int_{t=5.9\,\mathrm{s}}^{t_{\mathrm{zero}}} a\,\mathrm{d}t = -2.1 \times 10^{-1}\ \mathrm{m\,s^{-1}}, \quad \Delta V_2 = \int_{t_{\mathrm{zero}}}^{6.6\,\mathrm{s}} a\,\mathrm{d}t = 4.3 \times 10^{-2}\ \mathrm{m\,s^{-1}}$$

where a is the averaged acceleration signal, and t_{zero} is the time value of the zero-crossing of the acceleration after the peak. For the raw, unaveraged accelerations, these measures deviate by less than 6%. For the model signal these values are $\Delta V_1 = -2.0 \times 10^{-1}\,\mathrm{m\,s^{-1}}$ and $\Delta V_2 = 4.4 \times 10^{-2}\,\mathrm{m\,s^{-1}}$. To quantify the effect of broadening the peak acceleration, an even broader representation of the peak was tried. This is shown as the thin line in figure 10 and has the same values of ΔV_1 and ΔV_2 as the model signal used here. For these two signals, the surface profiles of figure 11 differed by less than 1.2%, measured as the mean absolute deviation between surface elevations normalized by the undisturbed depth. The value of maximum run-up during the impact with the wall differed by 1.4%. The results therefore seem to be rather insensitive to the actual shape of the modelling signal, as long as ΔV_1 and ΔV_2 are reasonably modelled.

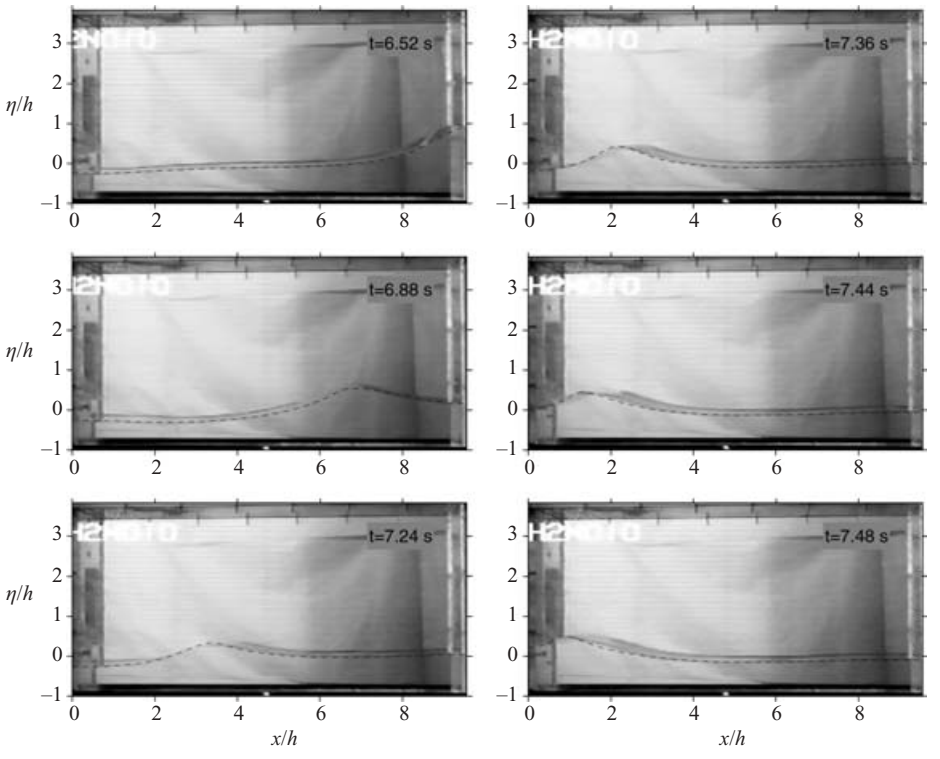

FIGURE 11. See facing page for caption.

In considering the maximum run-up, we are well beyond the range of validity of the Boussinesq equations. Since the basic approximation is based on shallow water and gentle slopes these equations cannot be expected to hold once the surface slope reaches $\frac{1}{4}\pi$. Nevertheless we have run the computations beyond that point and illustrate that the result is poor. To simulate the experimental flow conditions, the Boussinesq model was run using 102 grid points, a time step of 0.005 s, and with smoothing applied after each time step.

Computation with half the number of points gave essentially identical results until run-up. On the coarse grid, a reduction of the smoothing frequency by a factor of 100 caused little change in the solution. The mean deviation of these results from the results presented here is less than 1% of depth until run-up. The numerical solutions with differing numbers of points and smoothing gave noticeably different results only during and after the extreme run-up. For the results presented here, mass conservation applied with an accuracy of 4×10^{-5} relative to the total amount of water in the tank.

5.2. *Comparison of experimental and numerical results*

In figure 11 a selection of 12 frames from the regular-speed video is shown. The images cover the motion of the free water surface resulting from the push of the accelerating table, beginning with the situation of maximal elevation at the right-hand tank wall, and ending with the reflected wave generated after sloshing at the left-hand wall. On top of the images the numerical solution of the Boussinesq model is plotted as a dashed line. On most of the images, the free surface is seen as the region between two darker lines, which represent the intersection of the free surface with the front and back walls respectively. Numerical solutions are plotted in a coordinate system

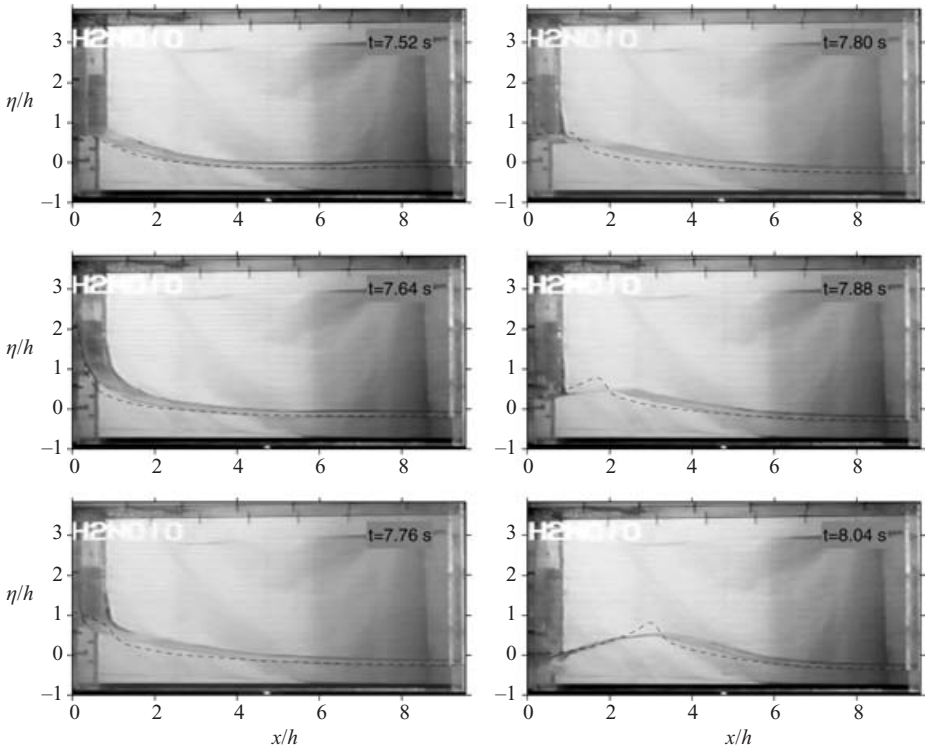

FIGURE 11. Comparison of numerical and experimental results, experiment H10 (Boussinesq solver). The numerical free-surface elevation is plotted as a dashed line. Time increases from top to bottom and from left to right. Time values are given in the upper right corner of each image.

fixed to the front wall of the tank, and therefore the lower dark line is the target when comparing the numerical results to the experimental profiles. For the present experiment, the regular-speed video camera was centred horizontally, and its vertical position was 200 mm above the tank floor with the tank in its rest position. This corresponds to the point $(x/h, z/h) = (4.7, 1.3)$.

Generally, the agreement between the experimental and numerical results is very good until the run up the wall. Comparing the second and third images of figure 11 ($t = 6.88$ s, 7.24 s), the wave loses height while travelling across the tank. On the following images, the wave is seen to steepen as it approaches the wall. These variations are probably due to the horizontal motion of the tank, creating waves longer than the corresponding solitary wave. Long shallow water waves steepen, and when dispersive effects are important they also increase in amplitude. The numerical prediction of the free-surface position is very good until $t = 7.64$ s when the model overpredicts the run-up at the wall. A careful analysis of the images reveals that the experimental run-up on the left wall is about $\eta/h = 1.8$ compared with a numerical run-up of $\eta/h = 2.5$. However, given our small-slope approximation and the near-vertical surface slope at maximum run-up, the computed result is not very different from the experiment. The effects of surface tension also influence the tip of the run-up in the experiment. The results of Jervis & Peregrine (1996) indicate that there could be an experimental shortfall of perhaps $0.1h$ due to surface tension in this case.

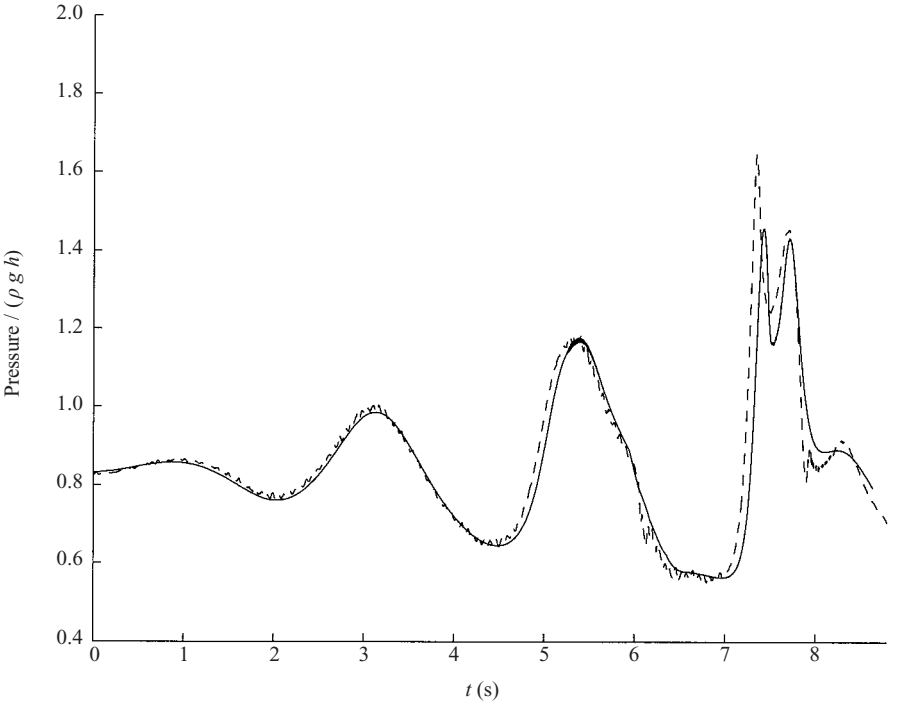

FIGURE 12. Comparison of measured (- - -) and calculated (——) pressure, experiment H10 (Boussinesq solver).

On the other hand, when compared with the images of the reflected wave in figure 11 for $t > 7.64$ s, the Boussinesq model is seen to produce a wave which is too high and characterized by a short, local crest. Although the numerical surface elevation has the general overall shape of the experimental profiles, this wave crest is not observed in the experimental data. As already indicated we believe these differences are mainly due to the failure of the model's gentle-slope approximation in the wave motion at the wall. In addition, the downward jet observed in figure 4 is not reproduced by the model.

5.3. *Comparison of pressure measurements*

During the experiment the pressure at the left-hand tank wall was measured using 8 pressure transducers mounted at different positions on the wall. Unfortunately, most of the pressure measurements are of poor quality, and we therefore only present results from a single transducer, positioned 26 mm above the bed at the middle of the wall. This transducer gave reliable measurements. In figure 12 the measured pressure is compared with the numerical results, obtained using equation (4.24). The numerical prediction compares well with the experimental results. All the qualitative trends are reproduced by the numerical results, even though small differences and a small phase shift are observed. As expected, the largest differences are seen close to the peaks of the pressure signal as the wave hits the wall. The double peak occurring at the impact with the wall is normal for strong wave impacts, and represents the pressure needed, first to accelerate the water up the wall and subsequently to slow down its descent.

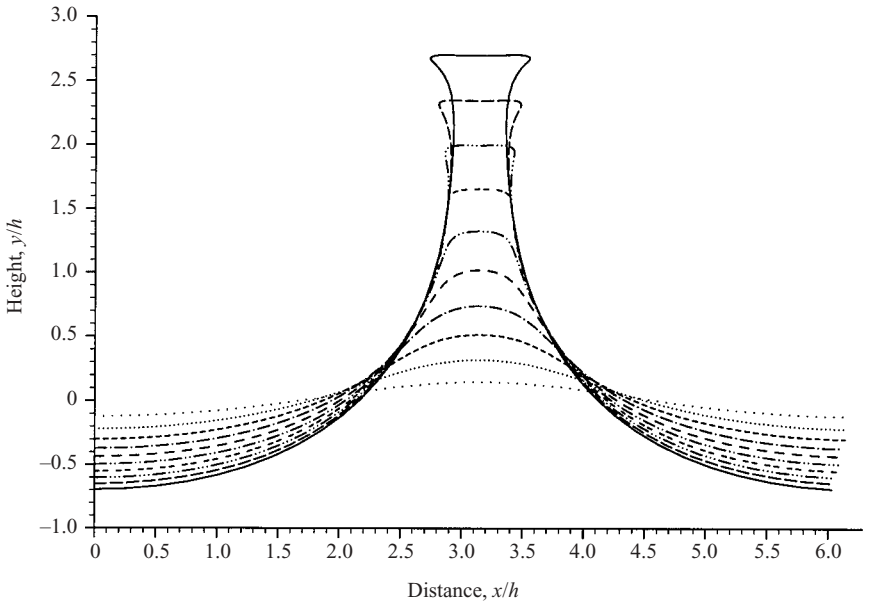

FIGURE 13. Surface profiles of 'standing waves' at maximum elevation for a sequence of different initial amplitudes for a cosine surface velocity distribution and initial uniform water depth of $h = 1$, $L = 2\pi$ (after Topliss 1994).

6. Numerical results for vertical shaking

In this section we present numerical results for the vertically forced experiments. As a typical example of such numerical modelling we present results for the experiment labelled V21 for which the water depth was 0.302 m. We present both the numerical results obtained with the Boussinesq model and the results obtained by continuing the calculations with a fully nonlinear irrotational flow solver.

'Table-top' crests have already been found numerically in Bristol (e.g. Topliss 1994) using a Cauchy boundary integral method for steep, unsteady two-dimensional waves (Dold & Peregrine 1986; Dold 1992) with high-energy initial conditions. A set of examples is shown in figure 13, where each curve represents the free surface at the time of maximum elevation for a set of systematically differing initial conditions.

We also present results of sample computations with this fully nonlinear irrotational flow solver in the last part of the section. Unlike the results of Topliss (1994), our numerical 'table-top' waves are obtained, like the experimental waves, with a varying vertical acceleration field rather than large initial amplitudes of surface elevation and velocity.

6.1. *Acceleration of the tank*

The driving signal for experiment V21 is of type 'V' (see figure 2), consisting of a small horizontal shaking of the tank, followed by a vertically oscillating motion. The acceleration measured is shown in figure 14, along with the acceleration used in the numerical modelling. The accelerations were sampled with a time step of 0.02 s, and the signals shown here are averaged with a moving window of 3 points for the horizontal accelerations and 2 points for the vertical acceleration. The signal used for modelling is based on the analytical expressions for the driving signals, adjusted to match the measured acceleration. A small peak followed by a decaying acceleration

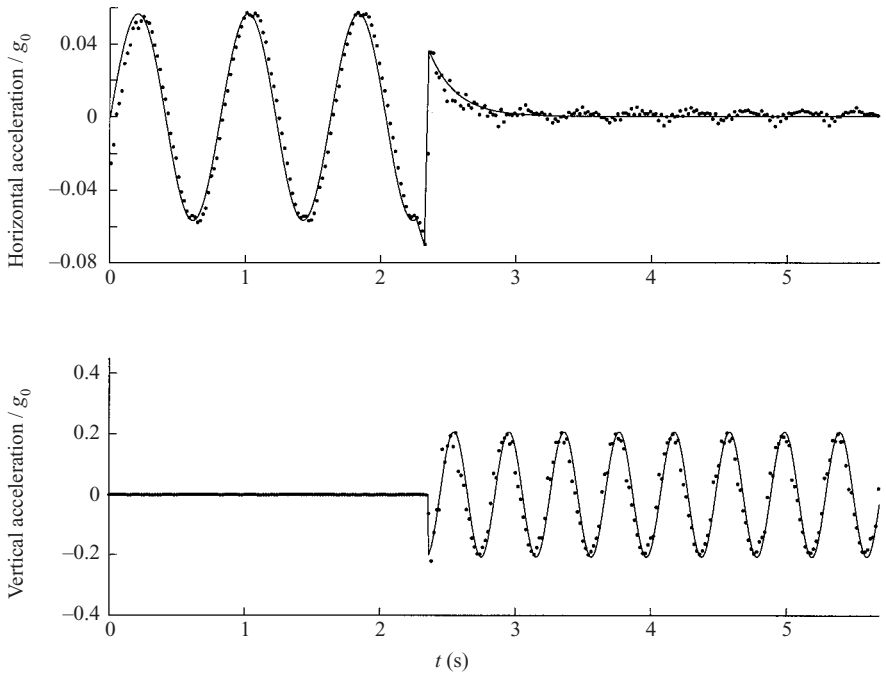

FIGURE 14. Tank accelerations for experiment V21: ···, measured; ——, modelling signal.

is seen in the horizontal signal around $t = 2.3$ s. This is due to the sudden stop of the horizontal motion before the vertical motion begins. After the horizontal motion is stopped, a small horizontal acceleration in phase with the vertical movement of the tank is measured. This acceleration is regarded as spurious, induced by the vertical motion on the horizontal accelerometer.

When simulating experiment V21, the Boussinesq solver was run with 102 grid points and with a time step of 0.005 s. Smoothing was applied after every 81 time steps, corresponding to half the linear period of the wave mode in the tank. Results with both half and twice as many points are very close, except for the final frames after the approximations involved have become questionable.

6.2. *Comparison of experimental and numerical results*

In figure 15 fourteen images of the wave motion are shown with the corresponding numerical solution plotted on top. The first seven images cover one half-period of the motion between two instants of maximum crest elevation. The results of the Boussinesq model compare very well with the experimental surface profiles.

The next half-period of motion is shown in images 7 to 13 of figure 15. The waves are now much steeper and the motion more nonlinear. The Boussinesq model still gives an acceptable prediction of the free-surface shape, though not as good as in the previous half-period. The last image in the figure shows the free-surface elevation at $t = 5.76$ s, one half-period later in the motion. The height of the standing wave is now overpredicted. After this instant, the simulation broke down during the downward motion of the wave crest at $t = 5.92$ s due to a numerical instability. The overpredictions occur after waves reach maximum surface slopes around $\frac{1}{4}\pi$, when the Boussinesq model is expected to have errors.

6.3. *Continuation of the computations with an irrotational flow solver*

In order to improve the modelling of the steep forced waves, the computations of the Boussinesq solver were extended by using a fully nonlinear irrotational flow solver. We used the program of Dold & Peregrine (1986), see also Dold (1992). It is based on using Cauchy's integral theorem for solving Laplace's equation, with high-order spatial and temporal accuracy. The present implementation solves the flow problem with periodic boundary conditions. The reader is referred to Dold (1992) for further details. As with the Boussinesq solver, the vertical shaking of the tank was modelled through a time-dependent acceleration field. The program was adapted accordingly, keeping the high order of numerical approximations.

As a measure of the difference in computational efficiency of the two models, we note that calculation of one period of the standing wave test of § 4.5 using 64 points took 14 CPU seconds on a Sun UltraSparc 2200 with the irrotational flow solver and 3 CPU seconds with the Boussinesq solver. This difference increases with the number of spatial points, since the Boussinesq solver requires $O(N)$ computational effort per time step, while the irrotational flow solver requires $O(N^2)$, N being the number of spatial discretization points.

The irrotational flow solver requires, as initial data, specification of the free surface elevation and the velocity potential on the free surface. While the free-surface elevation is directly available as one of the dependent variables of the Boussinesq model, the potential at the free surface was estimated by evaluating the line integral

$$\phi(x, \eta(x)) = \int_{x_0}^{x} \boldsymbol{V}(\xi, \eta(\xi)) \cdot (1, \eta'(\xi))\, \mathrm{d}\xi \tag{6.1}$$

where $\boldsymbol{V}(\xi, \eta(\xi)) = (u, w)$ is calculated from (4.22) and (4.23). To reduce the error induced in this evaluation, the solution of the Boussinesq solver was taken at a time of maximum surface elevation. For such instants, most of the wave energy is potential energy, related to $\eta(x)$, since the fluid velocity is near zero.

To continue the calculations for experiment V21, the solution of the Boussinesq solver was transferred to the irrotational flow solver at $t = 2.84$ s. This is shortly after the transition from horizontal to vertical shaking, thus providing a relatively gentle initial wave profile. In both models 81 computational points were used to resolve the tank length. To proceed beyond time $t = 5.85$ s it proved necessary to introduce smoothing of the solution. For the results shown here, a five-point smoothing formula was applied after each time step. The influence of smoothing was investigated by examining profiles of extreme elevation of $t = 5.36$ s and $t = 5.76$ s calculated with and without smoothing. The largest deviation was a reduction of the free crest height of 2.5% for $t = 5.36$ s. The influence of grid spacing was tested by carrying out a similar run with twice as many grid points. This run broke down at $t = 6.83$ s. For the profile of maximum crest elevation at $t = 6.60$ s, the largest deviation between the refined run and the results presented here, occurred at the right-hand tank wall, where the refined run predicted a crest height 3.9% greater.

The numerical results are compared to experimental observations beyond those of figure 15 in figure 16. The first five frames show instants of maximum crest elevations, while the last four frames depict the upward motion of the following crest, reaching its maximum height at $t = 8.32$ s. The numerical solutions compare very well with the experimental surface profiles. For $t \geqslant 7.44$ s near-breaking effects are observed at the wave crest and trough in the experimental results. These effects are beyond the scope of the numerical model, but still the wave heights are predicted well. In the last

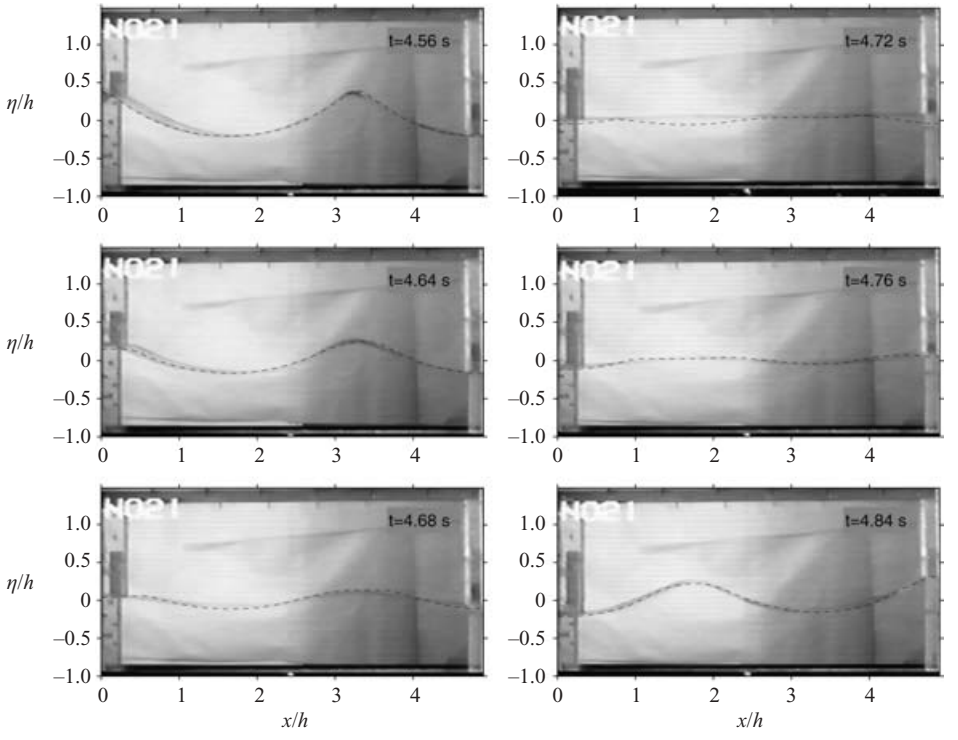

FIGURE 15. See facing page for caption.

four frames, surface disturbance around a flat-shaped crest can be seen. Although the model does not capture the square shape of the crest accurately, the overall shape of the wave is well modelled.

Here we are testing the limits of both the irrotational computation and the experimental measurements. The computation has been extended by introducing smoothing, which introduces slight errors, but prevents short grid-point-scale disturbances upsetting the computation. Similarly, the water surface is also sensitive to small-scale disturbances. Often these first appear in the boundary layer on the walls. Unfortunately, for these particular experiments, we have no oblique views to see the full transverse extent of the surface disturbances.

6.4. *Sample computations with vertical forcing*

Numerical modelling of the 'table-top' waves observed experimentally was not possible since all such waves were preceded by sharp wave crests which limited the continuation of computations. Hence we present here sample computations with the irrotational flow solver. Instead of pursuing a consistent reproduction of a given experiment, a linear standing wave was used as initial condition for the irrotational flow solver, still simulating the shaking of the tank through a time-dependent acceleration field. This method of simulating 'table-top' waves provides a cleaner and faster numerical setup, making parametric studies easier.

The experimental conditions of experiment V05 were used as the basis for the sample computations to reproduce the experimental observations discussed in § 3. Hence for a depth of $h = 0.40$ m, and wavelength $L = \frac{2}{3}L_{\text{tank}} = 0.987$ m the initial conditions

$$\eta(x) = ah\cos kx, \quad \phi(x, \eta(x)) = 0, \quad 0 \leqslant x \leqslant L, \tag{6.2}$$

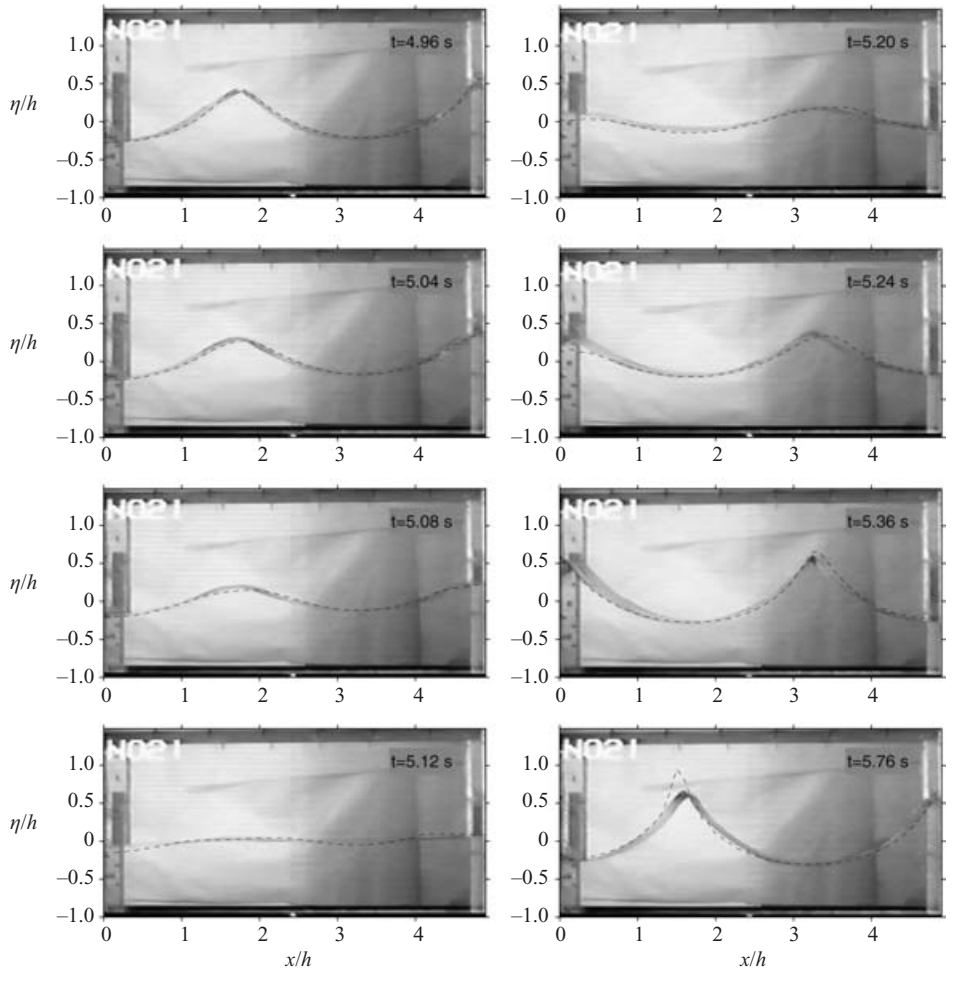

FIGURE 15. Comparison of numerical and experimental results, experiment V21 (Boussinesq solver). The numerical free-surface elevation is plotted as a dashed line. Time values are written in the upper right corner of each image.

were used, where $k = 2\pi/L$. The acceleration field was varied in time as

$$g(t) = g_0(1 + f \sin \omega t), \tag{6.3}$$

ω being twice the linear angular frequency of the corresponding standing wave mode. In the calculations neither smoothing nor surface tension was included. At the scale investigated here, surface tension is not important until sharp corners are approached and our numerical scheme fails. For $a = 0.3$ and $f = 0.75$ the result of a model run is presented in figure 17, obtained with 80 computational points. The resulting wave is seen to have the 'table-top' form observed experimentally. Figure 17(a) shows the upward motion of the wave, beginning with the initial condition (6.2). The wave reaches a 'table-top' shape early in its evolution, the top becoming perfectly flat and the sides almost vertical at $t = 0.34$ s. On further upward motion corners develop, so that the top of the profile is wider than the lower part. For the extreme profile the top has a small depression in the middle. For this profile the maximum surface elevation

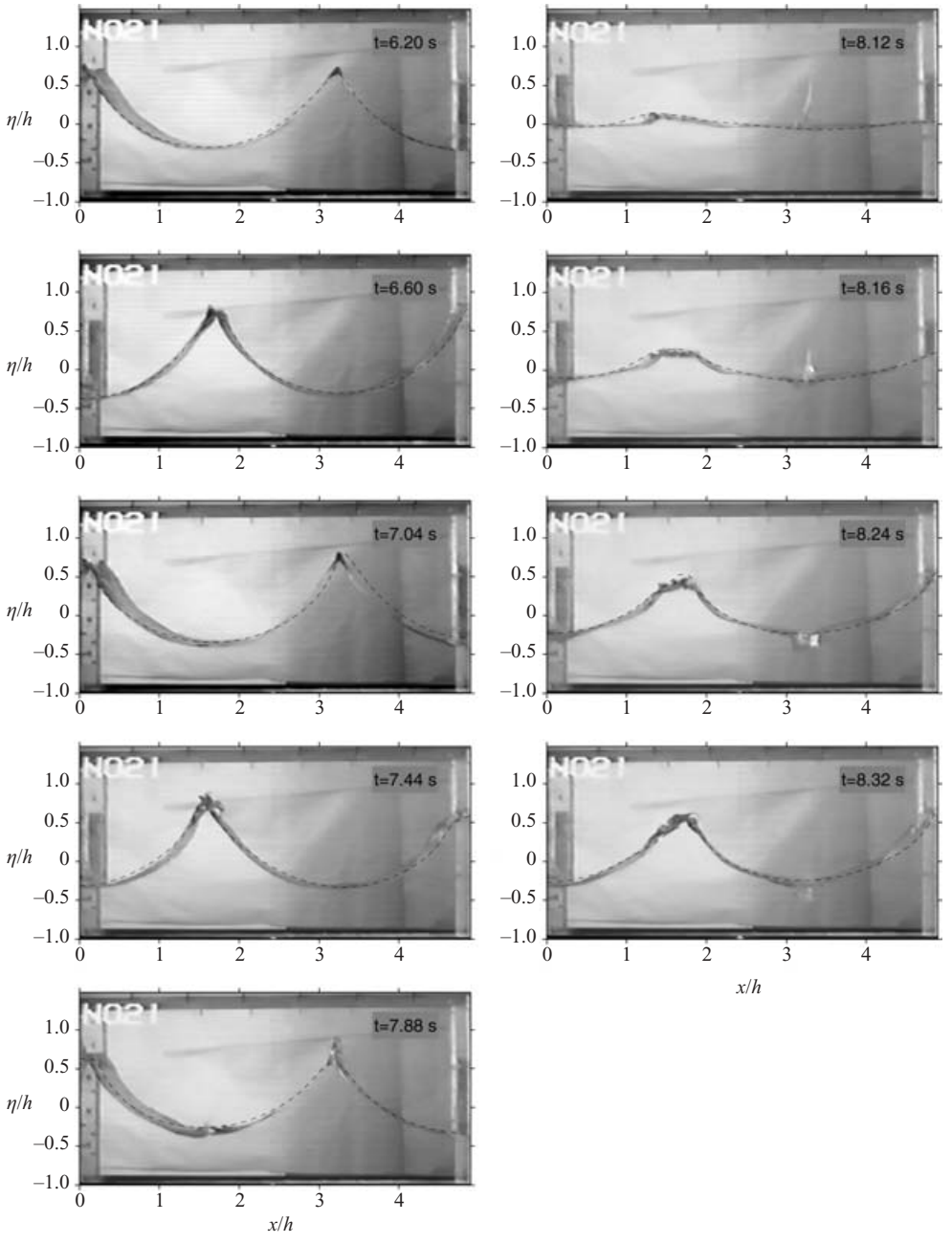

FIGURE 16. Comparison of experimental results and numerical results of an irrotational flow solver, experiment V21. The numerical free-surface elevation is plotted as a dashed line. Time values are given in the upper right corner of each image.

is $\eta_{\max}/h = 0.88$ and the height-to-thickness aspect ratio is 4.99, measured as the ratio of $\eta_{\max} - \eta_{\min}$ to the thinnest width of the profile.

At the transition to downward motion, the widening of the top continues, and furthermore the sides of the 'table top' become thinner. While the top has an almost

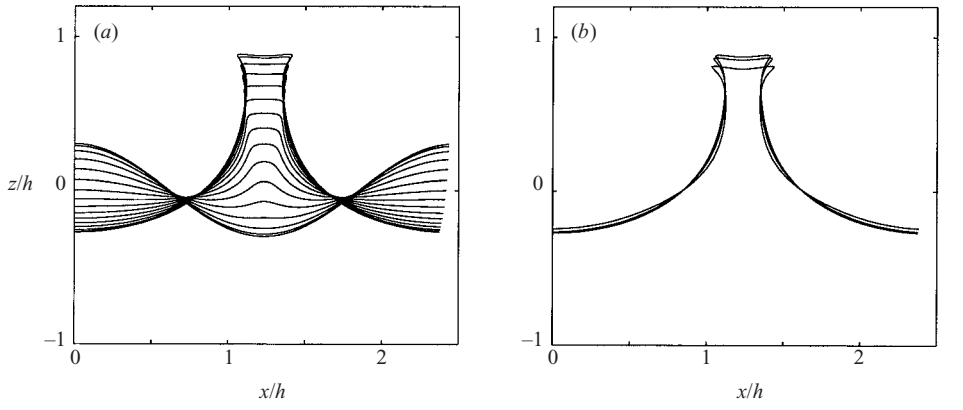

FIGURE 17. Free-surface elevation for a sample computation reflecting the experimental conditions of experiment V05. (*a*) The upward motion for the time values $t = 0.01\,\text{s}, 0.04\,\text{s}, \ldots, 0.46\,\text{s}$; (*b*) the downward motion for the time values $t = 0.46\,\text{s}, 0.49\,\text{s}, 0.52\,\text{s}$.

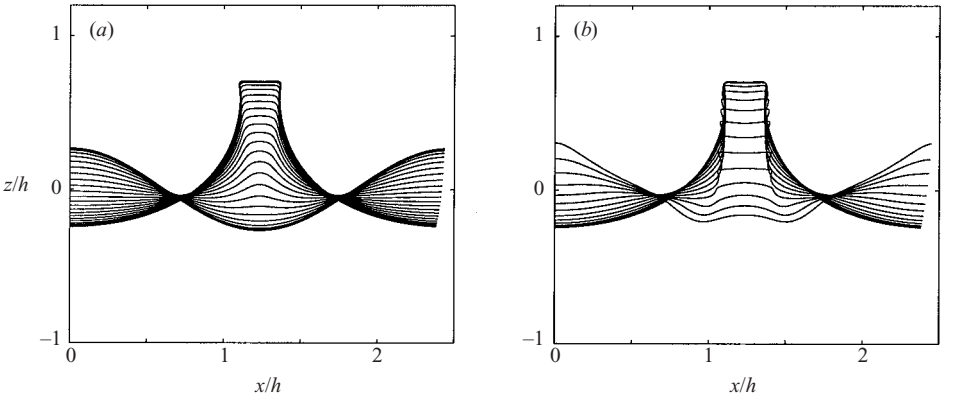

FIGURE 18. Upward and downward motion of a 'table-top' wave. (*a*) The upward motion for $t = 0\,\text{s}, 0.02\,\text{s}, \ldots, 0.44\,\text{s}$; (*b*) the downward motion for the time values $t = 0.44\,\text{s}$, $0.46\,\text{s}, \ldots, 0.70\,\text{s}$.

constant level of elevation for $t = 0.43$, 0.46 and 0.49 s, the sides are constantly moving inwards. This process is continued in the downward motion, as can be seen for the profile corresponding to $t = 0.52$ s. Stronger thinning processes of this type were observed experimentally.

Computation of this example broke down shortly after the time of the last profile shown. Thus, the complete downward motion of this 'table-top' wave could not be followed. However for a lower wave with an initial profile height of $a = 0.27$ and forcing of $f = 0.63$, using 80 computational points and five-point smoothing after every time step, figure 18 was obtained. The upward motion of the wave is very similar to that reported in figure 17, except for the reduced height. The profile of maximum elevation does not show corners and the top of the profile does not have a depression like in figure 18. Also, we see no thinning for this smaller wave. Additional computations show that the lack of thinning is not due to the numerical smoothing applied. The downward motion is interesting. The shape of the crest is almost

unchanged as the wave height decreases, with the slight overhang diminishing rather than leading to breaking. This is in agreement with the experimental observations of § 3. In particular, note that for irrotational flows time can be reversed and the downward motion in figure 17 is remarkably similar to the upward motion in figures 5.

7. Discussion and conclusion

Steep forced waves generated by moving a tank containing water have been studied both experimentally and numerically.

Experimental observation of waves generated in a horizontally accelerated tank were intended to reveal properties of the nature of violent wave impacts with water accelerations much greater than g, see e.g. Cooker & Peregrine (1992), but limitations of equipment meant that we only report on a strong wave impact here. Even so, this involved the wave crest rising high up the wall, forming a thin sheet of water that falls back down, creating a second pressure peak.

More striking observations have been achieved from forcing the wave motion with vertical acceleration. The most unusual feature is what we call a 'table-top' breaker. This is a flat-topped wave crest with almost vertical sides (a more energetic version of the 'mode B' breaker reported by J98). These energetic waves are characterized by sustaining a flat top through the rise and fall of the crest. For some of the 'table-top' breakers, we observe a thinning of the profile during the downward motion.

The more commonly seen steep sharp crests, 'mode A' of J98, are also evident. They also tend towards thin sheets of water as they fall. These sheets can lead to bubble entrainment, as with the initial motion of a jet directed towards the water surface, or because they can break up into drops that entrain bubbles on impact. Our videos show numerous other strong motions after the waves have broken, but reporting on these is beyond the scope of the present study.

To simulate the experimental results, the Boussinesq model of Wei *et al.* (1995) has been extended to include external acceleration. Boundary conditions taking the external acceleration into account have also been developed. The model is easily extended to three-dimensional motion. In all cases the Boussinesq model reproduces the free-surface motions accurately until the wave surface slopes are close to unity. After such steep waves occurred, wave crest amplitudes tended to be overpredicted. Numerical surface profiles compare well with the experimental profiles up to values of η as large as $\eta \approx 0.6h$. A comparison of experimental pressure measurements to numerical results of the Boussinesq solver shows similar good agreement.

The numerical modelling was taken to and beyond the extremes of validity of the model equations and of the numerical approximations. The Boussinesq-type equations are attractive since they require less computation, which is very important for extensions to three-dimensional waves. On the other hand, we note that a substantial amount of smoothing was required, especially for the travelling waves arising in H10. Further numerical schemes for these equations should be investigated. Also, high-order Boussinesq models such as that of Madsen, Bingham & Schäffer (2003*b*) could be chosen for a possible improvement of the accuracy and extension of the physical simulation time.

We continued the modelling of the vertically forced water waves beyond the applicability of the Boussinesq solver by using a fully nonlinear irrotational flow solver: data obtained from the Boussinesq solver were transferred (in an early stage of the experiment) to the irrotational flow solver, which ran until breakdown of

the computations due to limited resolution of sharp features. The results of these computations agree well with the experimental results.

Further interesting results have been obtained by carrying out sample computations with a sinusoidal free-surface elevation as initial condition for the potential flow solver with a time-varying vertical acceleration field. This generated 'table-top' waves similar to those observed in experiments, which could not be directly modelled since computations were limited by preceding sharp crests. For a smaller 'table-top' wave, the downward motion has also been followed, reproducing some experimental results, in which the wave profile is seen to move vertically downward almost unchanged.

We acknowledge assistance of Dr C. A. Taylor and Mr P. D. Greening of the Civil Engineering Department of Bristol University. Professor A. J. Roberts and Dr D. Smith, Department of Mathematics and Computing, University of Southern Queensland are acknowledged for supplying accurate standing wave profiles. Professor P. S. Larsen and Dr U. Ullum, Fluid Mechanics Section, Department of Mechanical Engineering, Technical University of Denmark, are thanked for use of video equipment. This research was supported by the EPSRC under contract number GR/H/96836. One of us, L. Thais, was also supported by the EU, DG: XII, contract number MAS2-CT94-5025.

REFERENCES

Abramson, H. N. 1966 The dynamic behaviour of liquids in moving containers. *NASA SP* 106.

Anderson, A., Diver, D. A. & Peregrine, D. H. 1990 Slender, steep and breaking water waves. In *Proc. 5th Intl Workshop on Water Waves and Floating Bodies* (ed. P. A. Martin), pp. 8–13. Manchester University. (http://www.rina.org.uk./showarticle.pl?id=6330&n=560&toparticle=6330).

Benjamin, T. B. & Ursell, F. 1954 The stability of the plane free surface of a liquid in vertical periodic motion. *Proc. R. Soc. Lond.* A **225**, 505–515.

Brocchini, M., Peregrine, D. H. & Thais, L. 1997 Violent free-surface motion: some wave-tank experiments. *Tech. Rep.* AM-97-01. School of Mathematics, University of Bristol.

Chan, E. S. 1994 Mechanics of deep-water plunging-wave impacts on vertical structures. *Coast. Engng* **22**, 115–133.

Chester, W. & Bones, J. A. 1968 Resonant oscillations of water waves. II. Experiment. *Proc. R. Soc. Lond.* A **306**, 23–39.

Cooker, M. J. & Peregrine, D. H. 1992 Wave impact pressure and its effect upon bodies lying on the bed. *Coastal Engng* **18**, 205–229.

Cooker, M. J. & Peregrine, D. H. 1995 Pressure-impulse theory for liquid impact problems. *J. Fluid Mech.* **297**, 193–214.

Cummings, P. D. & Chanson, H. 1999 An experimental study of individual air bubble entrainment at a planar plunging jet. *Chem. Engng Res. Design* **77** (A2), 159–164.

Dold, J. 1992 An efficient surface integral algorithm applied to unsteady gravity waves. *J. Computat. Phys.* **103**, 90–115.

Dold, J. W. & Peregrine, D. H. 1986 An efficient boundary-integral method for steep unsteady water waves. In *Numerical Methods for Fluid Dynamics* (ed. K. W. Morton & M. J. Baines). Oxford University Press.

Ervine, D. A. & Falvey, H. T. 1987 Behaviour of turbulent water jets in the atmosphere and in plunge pools. *Proc. Inst. Civ. Engrs* **83**, 295–314.

Faltinsen, O. M., Rognebakke, O. F., Lukovsky, I. A. & Timokha, A. N. 2000 Multidimensional modal analysis of nonlinear sloshing in a rectangular tank with finite water depth. *J. Fluid Mech.* **407**, 201–234.

Gobbi, M. F., Kirby, J. T. & Wei, G. 2000 A fully nonlinear Boussinesq model for surface waves. Part 2. Extension to $O(kh)^4$. *J. Fluid Mech.* **405**, 181–210.

Goodridge, C. L., Hentschel, H. G. E. & Lathrop, D. P. 1999 Breaking Faraday waves: critical slowing of droplet ejection rates. *Phys. Rev. Lett.* **82**, 3062–3065.

Hattori, M., Arami, A. & Yui, T. 1994 Wave impact pressure on vertical walls under breaking waves of various types. *Coastal Engng* **22**, 79–114.

Jervis, M. & Peregrine, D. H. 1996 Overtopping of waves at a sea wall: A theoretical approach. In *Proc. 25th Intl. Conf. Coastal Engng*, vol. 2, pp. 2192–2205. ASCE.

Jiang, L., Perlin, M. & Schultz, W. W. 1998 Period tripling and energy dissipation of breaking standing waves. *J. Fluid Mech.* **369**, 273–299 (referred to herein as J98).

Longuet-Higgins, M. S. 2000 Theory of water waves derived from a Lagrangian. Part 1. Standing waves. *J. Fluid Mech.* **423**, 275–292.

Longuet-Higgins, M. S. 2001 Vertical jets from standing waves. *Proc. R. Soc. Lond.* A **457**, 495–510.

Longuet-Higgins, M. S. & Cokelet, E. D. 1976 The deformation of steep surface waves on water. I. A numerical method of computation. *Phil. Trans. R. Soc. Lond.* A **350**, 1–26.

Longuet-Higgins, M. S. & Dommermuth, D. G. 2001*a* On the breaking of standing waves by falling jets. *Phys. Fluids* **13**, 1652–1659.

Longuet-Higgins, M. S. & Dommermuth, D. G. 2001*b* Vertical jets from standing waves II. *Proc. R. Soc. Lond.* A **457**, 2137–2149.

Longuet-Higgins, M. S. & Drazen, D. A. 2002 On steep gravity waves meeting a vertical wall: a triple instability. *J. Fluid Mech.* **466**, 305–318.

McIver, P. & Peregrine, D. H. 1981 Comparison of numerical and analytical results for waves that are starting to break. In *Proc. Conf. Hydrodynamics in Ocean Engng, Trondheim*, pp. 203–215.

Madsen, P. A., Bingham, H. B. & Liu, H. 2002*a* A new Boussinesq method for fully nonlinear waves from shallow water to deep water. *J. Fluid Mech.* **462**, 1–30.

Madsen, P. A., Bingham, H. B. & Schäffer, H. A. 2003 Boussinesq-type formulations for fully nonlinear and extremely dispersive water waves: Derivation and analysis. *Proc. R. Soc. Lond.* A **459**, 1075–1104.

Madsen, P. A. & Schäffer, H. A. 1999 A review of Boussinesq-type equations for gravity waves. In *Advances in Coastal and Ocean Engng* (ed. P. L.-F. Liu), vol. 5. World Scientific Publishing.

Mei, C. C. 1983 *The Applied Dynamics of Ocean Surface Waves*. John Wiley and Sons.

Mercer, G. N. & Roberts, A. J. 1992 Standing waves in deep water: their stability and extreme form. *Phys. Fluids* A **4**, 259–269.

Mercer, G. N. & Roberts, A. J. 1994 The form of standing waves on finite water depth. *Wave Motion* **19**, 233–244.

Miles, J. & Henderson, D. 1990 Parametrically forced surface waves. *Annu. Rev. Fluid Mech.* **22**, 143–165.

Mir, R. A. & Taylor, C. A. 1995 Experimental investigation into earthquake-induced failure of medium to low height concrete gravity dams. *Earthquake Engng Structural Dyn.* **24**, 373–393.

Nwogu, O. 1993 An alternative form of the Boussinesq equations for nearshore wave propagation. *J. Waterway Port Coastal Ocean Engng* **119**, 618–638.

Suchithra, N. & Koola, P. M. 1995 A study of wave impact on horizontal slabs. *Ocean Engng* **22**, 687–697.

Tilman, T. 1993 Nonlinear standing waves. PhD Dissertation, Technion, Haifa, Israel (mostly in Hebrew.)

Topliss, M. E. 1994 Water wave impact on structures. PhD Dissertation, School of Mathematics, University of Bristol, UK.

Underhill, W. B., Lichter, S. & Bernoff, A. J. 1991 Modulated, frequency-locked, and chaotic cross-waves. *J. Fluid Mech.* **225**, 371–394.

Wei, G. & Kirby, J. T. 1995 A time dependent code for extended Boussinesq equations. *J. Waterway Port Coastal Ocean Engng* **121**, 251–261.

Wei, G., Kirby, J. T., Grilli, S. T. & Subramanya, R. 1995 A fully nonlinear Boussinesq model for surface waves. Part 1. Highly nonlinear unsteady waves. *J. Fluid Mech.* **294**, 71–92.

Wood, D. J. & Peregrine, D. H. 1996 Wave impact beneath a horizontal surface. In *Proc. 25th Intl Conf. Coastal Engng*, vol. 3, 2573–2583. ASCE.

Wood, D. J., Peregrine, D. H. & Bruce, T. 2000 Study of wave impact against a wall with pressure-impulse theory: Part 1, Trapped air. *J. Waterway, Port, Coastal Ocean Engng* **126**, 182–190.

Ye, Z. 1990 Experimental investigation of fluid pressures in partially liquid filled horizontal cylindrical tanks during impact. Master's thesis, Dep. Mech. Engng., Queens University, Kingston, Onatario, Canada.

Ye, Z. & Birk, A. M. 1994 Fluid pressures in partially liquid-filled horizontal cylindrical vessels undergoing impact aeration. *J. Pressure Vessel Technol.* **116**, 449–458.

Zhang, S., Yue, D. K. P. & Tanizawa, K. 1996 Simulation of plunging wave impact on a vertical wall. *J. Fluid Mech.* **327**, 221–254.

Zhu, Y. G., Oguz, H. N. & Prosperetti, A. 2000 On the mechanism of air entrainment by liquid jets at a free surface. *J. Fluid Mech.* **404**, 151–177.